International Journal of Heat and Mass Transfer 167 (2021) 120822

Contents lists available at ScienceDirect

International Journal of Heat and Mass Transfer

journal homepage: www.elsevier.com/locate/hmt

Laminar to turbulent flow transition inside the boundary layer adjacent to isothermal wall of natural convection flow in a cubical cavity

Xin Wen[a], Lian-Ping Wang[a,b,c,d,e,*], Zhaoli Guo[f], Dauren B. Zhakebayev[g]

[a] Department of Mechanical Engineering, 126 Spencer Laboratory, University of Delaware, Newark, Delaware 19716-3140, USA
[b] Guangdong Provincial Key Laboratory of Turbulence Research and Applications, Center for Complex Flows and Soft Matter Research and Department of Mechanics and Aerospace Engineering, Southern University of Science and Technology, Shenzhen 518055, Guangdong, China
[c] Center for Complex Flows and Soft Matter Research, Southern University of Science and Technology, Shenzhen 518055, Guangdong, China
[d] Guangdong Provincial Key Laboratory of Turbulence Research and Applications, Southern University of Science and Technology, Shenzhen 518055, Guangdong, China
[e] Guangdong-Hong Kong-Macao Joint Laboratory for Data-Driven Fluid Mechanics and Engineering Applications, Southern University of Science and Technology, Shenzhen 518055, China
[f] State Key Laboratory of Coal Combustion, Huazhong University of Science and Technology, Wuhan, P.R. China
[g] Al Farabi Kazskh National University, Almaty, Kazakhstan

ARTICLE INFO

Article history:
Received 20 April 2020
Revised 4 December 2020
Accepted 10 December 2020

Keywords:
Natural convection
Flow transition
DUGKS
Accurate implementation of boundary conditions

ABSTRACT

We investigate three-dimensional natural convection flow in an air-filled, differentially heated cubical cavity. The vertical wall on the left is heated and the vertical wall on the right is cooled, with the remaining four walls being adiabatic. We performed direct numerical simulations of the natural convection flow using discrete unified gas-kinetic scheme (DUGKS), with an improved implementation of boundary conditions. Thin boundary layers are developed along the two isothermal walls. The laminar to turbulent flow transition inside the boundary layers is studied in this paper. The simulations are conducted at three Rayleigh numbers of 1.5×10^9, 1.0×10^{10}, 1.0×10^{11} using nonuniform grids with resolution up to 320^3. The Prandtl number is fixed at 0.71. We provide a detailed analysis of the transition from laminar to turbulent flow inside the vertical boundary layers and its influence on the rate of heat transfer. Time traces of temperature and velocity, time-averaged flow field, statistics of fluctuation fields are presented to illustrate distinct behaviors in the laminar and turbulent thermal boundary layer, as well as to determine the transition location at different *Ra* numbers. The average Nusselt numbers for different *Ra* numbers are compiled and compared to previous results. A guideline of the resolution requirement is suggested based on the *Ra* scaling of laminar thermal boundary layer.

1. Introduction

Natural convection in an enclosure is a classical configuration in heat transfer research due to many applications such as such as cooling of the electronic device, energy storage system and climate conditioning of rooms [1]. Using convection to enhance heat transfer in a compact space is a highly effective approach. Based on the direction of the applied temperature gradient, it can be classified into two categories: cavity heated from below (Rayleigh-Bénard) and these differentially heated from the sides. The Rayleigh-Bénard convection has been widely studied [2,3], while the latter case is relatively less studied and is considered in this paper. Namely, here the left vertical wall of the cavity is heated and the right vertical wall is cooled, with the remaining four walls being kept adiabatic.

Researchers have studied this latter configuration for several decades, focusing on different aspects such as the instability mechanism of the convection and the Nusselt - Rayleigh number correlation, where the Rayleigh number is the key input parameter and the Nusselt number measures the dimensionless heat transfer rate, both will be defined in Section 2. Despite its simple configuration, this problem is extremely complex due to the strong coupling between velocity field and temperature field and a large range of system parameters such as the cavity aspect ratio, Prandtl number, temperature difference, etc. When the temperature differ-

* Corresponding author at: Guangdong Provincial Key Laboratory of Turbulence Research and Applications, Center for Complex Flows and Soft Matter Research and Department of Mechanics and Aerospace Engineering, Southern University of Science and Technology, Shenzhen 518055, Guangdong, China.
E-mail address: lwang@udel.edu (L.-P. Wang).

https://doi.org/10.1016/j.ijheatmasstransfer.2020.120822
0017-9310/

ence is small, the density change is negligible except in the buoyancy term. And under the Boussinesq assumption the fluid properties such as viscosity ν, heat conductivity k, are treated as constants. The viscous dissipation in the energy equation is typically neglected. Led by the pioneering work of de Vahl Davis and coworkers [4,5], researchers used different methods to study this problem numerically and provided benchmark solutions for both two- and three-dimensional cavities; and the simulation results were compared to earlier experimental results [6–8]. A summary of previous direct numerical simulations of natural convection in a differentially heated cavity related to our study is presented below.

Due to the restriction of the computational resource, the early numerical studies focused on steady laminar convection flow. For flow in a two-dimensional square cavity, de Vahl Davis and Jones [5] provided a set of benchmark solutions for the laminar regime ($10^3 \le Ra \le 10^6$) using the finite-difference method. Later, Quéré [9] used the pseudo-spectral method to solve the problem with finer meshes up to 128×128. He provided solutions for the full range of two-dimensional steady-state flow ($Ra \le 10^8$). Beyond a critical Ra, the two-dimensional natural convection flow becomes time-dependent, the onset of the unsteadiness is affected by several controlling parameters. Using the finite-difference method, Paolucci and Chenoweth [10] studied two-dimensional natural convection with Rayleigh number up to 10^{10} in cavities of aspect ratio near unity. They claimed that for cavity with aspect ratio (A=height/length) less than $\frac{1}{2}$ or larger than 3, the primary instability takes place insides the boundary layer along the isothermal wall. However, for $\frac{1}{2} < A < 3$ the instability first happens near the departing corners. Janssen and Henkes [11] performed two-dimensional simulations in a differentially heated square cavity with Prandtl number between 0.25 and 7.0. They found that for Prandtl number between 0.25 and 2.0, the flow exhibits periodic, quasi-periodic behaviors before becoming turbulent eventually. While for larger Prandtl number, flow goes from steady to turbulent without intermediate transition.

For an air-filled differentially heated square cavity with adiabatic horizontal walls, Quéré and Behnia [12] concluded that the critical Rayleigh number for transition from steady to unsteady flow is $Ra_{cr} = 1.82 \pm 0.01 \times 10^8$, using a relatively coarse mesh resolution at 72×72. They studied time-dependent flow up to $Ra = 1.0 \times 10^{10}$ in 2D, based on the pseudo-spectral Chebyshev algorithm. Two-dimensional natural convection flow in a square cavity can be a good approximation of the flow at the mid-plane of the three-dimensional cubical cavity. As stated by Janssen and Henkes [11], the boundary layer along the heated wall of the cavity resembles those along the isothermal vertical plate. However, the introduction of the top wall of the cavity changes the flow structure. The vertical boundary layer is turned horizontal and creates a jet-like fluid layer which induces the first instability. When the Rayleigh number is further increased, the second instability takes place insides the boundary layer. Although there are numerous studies about the boundary layer adjacent to an isothermally heated vertical surface [13,14], the introduction of the horizontal walls restrains the free development of the vertical boundary layer. As the heat transfer is highly affected by the flow regime of the thermal boundary layer, in this study we will focus on absolute instability of thermal boundary layer, specifically, the flow transition insides the boundary layers and its influence on the heat transfer. In passing we note that Janssen and Armfield [15] studied convective instability due to externally imposed perturbations within the thermal boundary layer. The convective instability occurs at a much smaller Rayleigh number than those at which the absolute instability happens.

As the turbulent convection flow must be essentially three-dimensional in nature, researchers extended DNS to the three-dimensional cavities based on previous two-dimensional studies. Mallinson and de Vahl Davis [4] performed an early simulation of three-dimensional natural convection using the finite-difference method with relatively coarse meshes for the Rayleigh number range $10^4 \le Ra \le 10^6$. Fusegi et al. [16] reported a finite-difference numerical study of three-dimensional natural convection in a cubical cavity for Rayleigh number range of $10^3 \le Ra \le 10^6$. Tric et al. [17] provided a set of benchmark solutions for $10^3 \le Ra \le 10^7$ using pseudo-spectral Chebyshev algorithm based on the projection-diffusion method. Fusegi et al. [18] reported benchmark results for $Ra = 10^{10}$ using $62 \times 122 \times 62$ meshes. With the introduction of the lateral walls in the third direction, we expect the critical Rayleigh number for the onset of unsteady convection will be affected by these lateral walls. Janssen and Henkes [19] studied the transition to unsteady flow in the three-dimensional cavity with adiabatic horizontal walls, and obtained the critical Ra between 2.5×10^8 and 3×10^8 by assuming symmetry so that they only performed simulation on a quarter of the cavity. However, Labrosse et al. [20] claimed that transition happens at $Ra = 3.19 \times 10^7$ without assuming symmetry.

In the current study, we perform three-dimensional simulations in a cubical cavity with a Rayleigh number range far beyond the critical Rayleigh number. This allows us to investigate the flow transition insides the boundary layer which is the second type of instability for this specific configuration. Another important research goal for natural convection is to predict the Nusselt number of the heated wall which is desired for engineering applications. Utilizing the numerical results for a large range of Rayleigh number, researchers proposed Rayleigh - Nusselt correlations for the three-dimensional cubical enclosure. Fusegi et al. [18] proposed an empirical correlation for the overall Nusselt number $Nu_{\text{overall}} = 0.163 Ra^{0.282}$ for $10^3 \le Ra \le 10^{10}$ with relatively coarse mesh. Wang [21], Wang et al. [22] reported the correlation $Nu_{\text{overall}} = 0.127 Ra^{0.3052}$ for steady flow regime $10^3 \le Ra < 10^7$ and $Nu_{\text{overall}} = 0.3408 Ra^{0.241}$ for unsteady flow regime $10^7 \le Ra \le 10^{10}$. While for the steady flow regime, the average Nusselt number results are in good agreement, the results have noticeable differences in the unsteady flow regime. One reason for this disagreement is that the high Rayleigh number convection requires fine mesh, and Fusegi used a relatively coarse mesh. For unsteady flow regime, the Nusselt - Rayleigh correlation still needs to be improved.

In general, three-dimensional differentially-heated natural convection flow in a cavity has a unique flow structure rather different from the Rayleigh-Bénard problem. Driven by the buoyancy force $\beta g(T - T_0)$ along the vertical direction, thin boundary layers develop along the isothermal walls, outside the boundary layer, the core region is quiescent and there is a vertical temperature stratification in the cavity center. In the previous studies, most researchers focused on general flow feature of the natural convection and provided a set of time-averaged statistics [6,17,18]. Only a few of them paid attention to the transition from laminar to turbulent flow insides the boundary layer. Trias et al. [23–25] performed direct numerical simulations to a differentially heated cavity of aspect ratio 4 up to $Ra = 10^{11}$ and provided a comparison between two- and three-dimensional results for this problem. They claimed that the thermal boundary layers of the three-dimensional flow remain laminar or quasi-laminar in the upstream parts, up to a point where the eddies are ejected. This transition location moves further upstream for 3D simulations, compared to 2D simulations. However, for the cubical cavity, the influence of the top and bottom wall is more significant. And based on the analysis of Paolucci and Chenoweth [10], the aspect ratio plays an important role in the development of flow instability, the instability mechanism of the cubic cavity is different from the tall cavity.

The primary goal of the current work is to improve our understanding of the transition from laminar to turbulent flow inside the vertical boundary layer in a differentially heated cubi-

cal cavity with adiabatic horizontal and lateral walls. In recent years, the kinetic method (or mesoscopic CFD method based on the model Boltzmann equation) has been developed and become a reliable tool for thermal flow simulations [26–28]. The discrete unified gas-kinetic scheme [29] is used for the current study. Comparisons of performance in terms of accuracy, stability, and efficiency have been done previously in Wang et al. [30,31] and Bo et al. [32]. Wang et al. [30] compared DUGKS and LBM in the simulation of lid-driven cavity flow, laminar flow past a square cylinder. Wang et al. [31] compared DUGKS, LBM, and spectral method in the simulation of decaying turbulent flows, Bo et al. [32] compared DUGKS, LBM, and spectral method in the simulation of 3D Taylor-Green vortex flow and wall-bounded channel flows. In these studies, the second-order accuracy has been demonstrated. In terms of efficiency, DUGKS is slower than LBE in terms of updating the distribution functions at the lattice nodes due to its additional evaluation of interface fluxes. However, as a finite volume scheme DUGKS can use a non-uniform mesh. As a result, if the non-uniform mesh can be clustered in the region with a large flow gradient, the efficiency of DUGKS can be better than LBM. The relative efficiency of DUGKS over LBM was discussed for the simulation of the flow passing the square cylinder in Wang et al. [30] and for turbulent channel flow in Bo et al. [32]. Non-uniform meshes can be easily implemented in this scheme and the boundary condition can be applied right at the cell interface on the wall. However, accurate implementation of temperature and velocity boundary conditions in the kinetic method remains a research topic, and here we will propose an improved implementation that is consistent with the Chapman-Enskog analysis. Different statistics will be used to specify the transition location, and study the influence of flow transition on the rate of heat transfer.

The present paper is organized as follows. The physical problem description and numerical method (DUGKS) are first presented in Section 2. Numerical results are presented to address several physical aspects. In Section 3.3 we discuss the time evolution of velocity and temperature of a set of selected monitoring points and their power spectra. Averaged flow fields are presented in Section 3.4, followed by secondary statistics in Section 3.5. The effect of flow transition on heat transfer is presented in Section 3.6. Finally, a summary is given in Section 4.

2. Governing equations and numerical methods

2.1. Problem description and governing equations

We consider an air-filled cubical cavity of height h, with an isothermal vertical hot wall at temperature $T_h = T_0 + 0.5\Delta T$ on the left, and a cold wall at temperature $T_c = T_0 - 0.5\Delta T$ on the right; where the temperature difference $\Delta T = T_h - T_c$ and the mean temperature $T_0 = (T_h + T_c)/2$. The other four walls (*i.e.*, two other vertical walls and two horizontal walls) are assumed to be adiabatic. No-slip velocity boundary conditions are imposed on all walls. Under the Boussinesq assumption, the fluid density is treated as a constant except with two considerations: (1) the buoyancy force is retained due to density variation caused by temperature change and (2) the volume expansion work in the thermal energy equation is retained under the ideal gas assumption Kundu et al. [33]. Furthermore, the viscous dissipation in the thermal energy equation is neglected as it is typically very small for the case of air under natural convection. The governing equations can then be written as

$$\nabla \cdot \boldsymbol{u} = 0, \tag{1a}$$

$$\rho \frac{\partial \boldsymbol{u}}{\partial t} + \rho(\boldsymbol{u}\cdot\nabla)\boldsymbol{u} = -\nabla p + \rho\nu\nabla^2\boldsymbol{u} - \rho\beta(T - T_0)\boldsymbol{g}, \tag{1b}$$

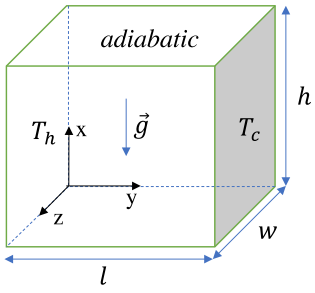

Fig. 1. The geometry under consideration.

$$\frac{\partial T}{\partial t} + (\boldsymbol{u}\cdot\nabla)T = \alpha\nabla^2 T, \tag{1c}$$

where $\boldsymbol{u}$ is the flow velocity, T is the temperature, ρ is the density at the mean temperature T_0, $\boldsymbol{g}$ is the gravitational acceleration, p is a modified pressure including the effect of mean body force $\rho\boldsymbol{g}$, ν is the kinematic viscosity, β is the thermal expansion coefficient, and α is the thermal diffusivity. Under the above Boussinesq assumption, the temperature field is treated as a scalar field which is advected by the macroscopic flow with a constant diffusion coefficient. Nevertheless, the velocity field and the temperature field are closely coupled: the flow is driven by the temperature field through the buoyancy force, and at the same time the temperature field is advected by the flow velocity. This coupling introduces another level of nonlinearity in addition to the inertial term in the momentum equation. The coordinate system used is: x is the vertical direction, y is the horizontal direction perpendicular to the heated wall, and z is the spanwise direction.

With the above setup and the simplified governing equations, the system is governed by the geometrical parameters (cavity height h,cavity length l, cavity depth w, see Fig. 1), fluid properties $(\nu, (\beta g), \alpha)$, the reference temperature T_0, and driving temperature difference ΔT. Note that the mean density can be absorbed into the pressure term thus it is not listed. Also (βg) is viewed as a single parameter as they appear together in the momentum equation. By dimensional analysis, it follows that the system is governed by the following five independent dimensional parameters

$$Ra \equiv \frac{g\beta\Delta T h^3}{\nu\alpha}, \quad Pr \equiv \frac{\nu}{\alpha}, \quad \frac{\Delta T}{T_0}, \quad \frac{h}{l}, \quad \frac{h}{w} \tag{2}$$

Furthermore, it is assumed that $\Delta T/T_0 << 1$. With the two aspect ratios h/l and h/w fixed to one here and the Prandtl number for air given as $Pr = 0.71$, the only governing parameter remaining is the Rayleigh number Ra, which can be interpreted as $Ra = Re_{\text{eff}}^2 Pr$, where the effective Reynolds number is defined as $Re_{\text{eff}} \equiv u_0 h/\nu$, with the buoyancy velocity defined as $u_0 = \sqrt{\beta\Delta T g h}$.

We can now nondimensionalize all quantities in the governing equations by the length scale h, velocity scale u_0, time scale h/u_0, pressure scale ρu_0^2 and temperature scale ΔT. Since the temperature equation is linear, a reference value can be subtracted, so we define the normalized temperature as $\theta = (T - T_0)/\Delta T$. The governing equations in the nondimensional form can then be written as

$$\nabla \cdot \hat{\boldsymbol{u}} = 0, \tag{3a}$$

$$\frac{\partial \hat{\boldsymbol{u}}}{\partial \hat{t}} + \left(\hat{\boldsymbol{u}}\cdot\nabla\right)\hat{\boldsymbol{u}} = -\nabla\hat{p} + \frac{Pr^{1/2}}{Ra^{1/2}}\nabla^2\hat{\boldsymbol{u}} + \theta\boldsymbol{e}_x, \tag{3b}$$

$$\frac{\partial \theta}{\partial \hat{t}} + \left(\hat{\boldsymbol{u}}\cdot\nabla\right)\theta = \frac{1}{Pr^{1/2}Ra^{1/2}}\nabla^2\theta, \tag{3c}$$

where $\hat{\boldsymbol{u}}$, $\hat{p}$ and $\hat{t}$ denote the normalized velocity, pressure and time, respectively, $\boldsymbol{e}_x$ is the unit vector pointing vertically upward.

The initial state of the flow is set to be quiescent $\hat{\boldsymbol{u}} = 0$ and isothermal $\theta = 0$. The velocity boundary condition is $\hat{\boldsymbol{u}} = 0$ on all walls, the thermal boundary conditions are: $\theta(y = 0) = 0.5$, $\theta(y = 1) = -0.5$, and zero normal temperature gradient on the other four walls.

2.2. Numerical method

In the present work, we perform numerical simulations using discrete unified gas-kinetic scheme (DUGKS), which is a recently developed finite-volume formulation of the model Boltzmann equation by Guo et al. [29], Wang et al. [34]. In this section, we introduce the gas-kinetic model based on the Bhatnagar-Gross-Krook (BGK) collision model in the incompressible limit and provide a brief description of DUGKS algorithm. Corresponding to the governing equations, the gas-kinetic equations can be constructed as [35]:

$$\frac{\partial f}{\partial t} + \boldsymbol{\xi}\cdot\nabla_{\boldsymbol{x}} f + \boldsymbol{a}\cdot\nabla_{\boldsymbol{\xi}} f = \Omega_f \equiv \frac{f^{eq} - f}{\tau_v}, \tag{4a}$$

$$\frac{\partial g}{\partial t} + \boldsymbol{\xi}\cdot\nabla_{\boldsymbol{x}} g = \Omega_g \equiv \frac{g^{eq} - g}{\tau_c}, \tag{4b}$$

where $f = f(\boldsymbol{x}, \boldsymbol{\xi}, t)$ and $g = g(\boldsymbol{x}, \boldsymbol{\xi}, t)$ are the distribution functions for velocity and temperature, respectively. Both functions are for particles moving with velocity $\boldsymbol{\xi}$ at position $\boldsymbol{x}$ and time t. The two equilibrium distributions f^{eq} and g^{eq} take the form of the Maxwellian equilibrium:

$$f^{eq} = \frac{\rho}{(2\pi RT_1)^{D/2}} exp\left(-\frac{(\boldsymbol{\xi}-\boldsymbol{u})^2}{2RT_1}\right), \tag{5a}$$

$$g^{eq} = \frac{T}{(2\pi RT_2)^{D/2}} exp\left(-\frac{(\boldsymbol{\xi}-\boldsymbol{u})^2}{2RT_2}\right), \tag{5b}$$

where R is gas constant, D is the spatial dimension, T_1 and T_2 are constants determining the effective speed of the sound. The two relaxation times τ_v and τ_c are related to the viscosity $\nu = \tau_v RT_1$ and thermal conductivity $\kappa = \tau_c RT_2$. By modifying these two relaxation times, the Prandtl number $Pr = \nu/\kappa$ can be adjusted. Under the Boussinesq approximation, the external force is given as $\boldsymbol{a} = g\beta[T - T_0]\boldsymbol{e}_x$.

In our simulation, in lattice units we set $RT_1 = RT_2 = 10$ and $u_0 = \sqrt{\beta g \Delta T h} = \sqrt{0.1}$ so that the Mach number $Ma = u_0/\sqrt{RT}$ is small enough to satisfy the incompressible limit. The maximum local Mach number in the simulation is around $Ma_{\max} = u_{\max}/\sqrt{RT} \approx 0.25$ for the high Rayleigh number cases. The time step in DUGKS is determined by the Courant-Friedrichs-Lewy (CFL) condition:

$$\Delta t = CFL\frac{\Delta x_{\min}}{\xi_{\max}} \tag{6}$$

where CFL number is set to be 0.5 for all simulations, $\Delta x_{\min}$ is the minimal grid spacing and $\xi_{\max}$ is the maximal discrete particle velocity. The hydrodynamic variables are computed by:

$$\rho = \int f d\boldsymbol{\xi}, \qquad \rho\boldsymbol{u} = \int \boldsymbol{\xi} f d\boldsymbol{\xi}, \qquad T = \int g d\boldsymbol{\xi}. \tag{7}$$

One way to include the external force term is to merge the force term into the collision term. The DUGKS can be constructed based on two kinetic equations, we rewrite Eq. (4) as:

$$\frac{\partial \phi}{\partial t} + \boldsymbol{\xi}\cdot\nabla_{\boldsymbol{x}}\phi = \Omega_m \equiv \Omega_\phi + F_{ext}, \tag{8}$$

where $\phi = g$ or h, $F_{ext} = 0$ for h distribution function. For the continuum flow regime, the Chapman-Enskog analysis implies that the external body force term F_{ext} for f can be approximated as [26]:

$$F_{ext} = -\boldsymbol{a}\cdot\nabla_{\boldsymbol{\xi}} f \approx -\boldsymbol{a}\cdot\nabla_{\boldsymbol{\xi}} f^{eq} = \frac{\boldsymbol{a}\cdot(\boldsymbol{\xi}-\boldsymbol{u})}{RT_1} f^{eq}. \tag{9}$$

As the DUGKS is a finite-volume scheme, the computational domain is divided into a set of control volumes. Integrating Eq. (8) over a control volume V_j centered at $\boldsymbol{x}_j$ from time t_n to t_{n+1}. The divergence theorem is applied to the convection term to convert the cell-volume integral to the cell-surface integral, then the midpoint rule is used to integrate the surface flux.

$$\begin{aligned}
&\frac{1}{V_j}\int\int_{t_n}^{t_{n+1}} \boldsymbol{\xi}\cdot\nabla_{\boldsymbol{x}}\phi(\boldsymbol{x}_j, \boldsymbol{\xi}, t_n) dt dV \\
&= \frac{1}{V_j}\int_{t_n}^{t_{n+1}}\int_{\partial V_j} (\boldsymbol{\xi}\cdot\boldsymbol{n})\phi(\boldsymbol{x}_j, \boldsymbol{\xi}, t_n) ds dt \\
&= \frac{\Delta t}{V_j}\int_{\partial V_j} (\boldsymbol{\xi}\cdot\boldsymbol{n})\phi(\boldsymbol{x}_j, \boldsymbol{\xi}, t_{n+1/2}) ds
\end{aligned} \tag{10}$$

The collision term is treated by the trapezoidal rule. The evolution equation for the velocity distribution can be written as:

$$\tilde{\phi}(\boldsymbol{x}_j, \boldsymbol{\xi}, t_{n+1}) = \tilde{\phi}^+(\boldsymbol{x}_j, \boldsymbol{\xi}, t_n) - \frac{\Delta t}{|V_j|} F_\phi(\boldsymbol{x}_b, \boldsymbol{\xi}, t_{n+1/2}), \tag{11}$$

where $\tilde{\phi}(\boldsymbol{x}_j, \boldsymbol{\xi}, t_{n+1})$ and $\tilde{\phi}^+(\boldsymbol{x}_j, \boldsymbol{\xi}, t_n)$ are auxiliary distribution functions introduced to remove implicity:

$$\tilde{\phi} = \phi - \frac{\Delta t}{2}\Omega_m, \quad \tilde{\phi}^+ = \phi + \frac{\Delta t}{2}\Omega_m. \tag{12}$$

The microscopic flux $F_\phi(\boldsymbol{x}_b, \boldsymbol{\xi}, t_{n+1/2})$ across the cell interface $\boldsymbol{x}_b$ at the half time step $t_{n+1/2}$ is defined as:

$$F_\phi(\boldsymbol{x}_b, \boldsymbol{\xi}, t_{n+1/2}) = \sum(\boldsymbol{\xi}\cdot\boldsymbol{n})\phi(\boldsymbol{x}_b, \boldsymbol{\xi}, t_{n+1/2}) d\boldsymbol{S}, \tag{13}$$

where $\phi(\boldsymbol{x}_b, \boldsymbol{\xi}, t_{n+1/2})$ is distribution function at cell interface $\boldsymbol{x}_b$ and half time step $t_{n+1/2}$. Since the auxiliary distributions are related to the original distribution function ϕ and equilibrium ϕ^{eq}, the conservative flow variables can be computed from $\tilde{\phi}$ directly. Thus we can track the evolution of the distribution function $\tilde{\phi}$ instead of original distribution function ϕ.

The key point of updating evolution equation Eq. (11) is to evaluate the net flux $F_\phi(\boldsymbol{x}_b, \boldsymbol{\xi}, t_{n+1/2})$ properly, which requires the reconstruction of the original distribution function $\phi(\boldsymbol{x}_b, \boldsymbol{\xi}, t_{n+1/2})$. Eq. (8) is integrated along characteristic line with the end point $(\boldsymbol{x}_b)$ from t_n to $t_n + h$ $(h = \Delta t/2)$, and the trapezoidal rule is applied to the collision term,

$$\begin{aligned}
&\phi(\boldsymbol{x}_b, \boldsymbol{\xi}, t_n + h) - \phi(\boldsymbol{x}_b - \boldsymbol{\xi}h, \boldsymbol{\xi}, t_n) \\
&= \frac{h}{2}\left[\Omega_m(\boldsymbol{x}_b, \boldsymbol{\xi}, t_n + h) + \Omega_m(\boldsymbol{x}_b - \boldsymbol{\xi}h, \boldsymbol{\xi}, t_n)\right].
\end{aligned} \tag{14}$$

In order to remove the implicity of Eq. (14), a second set of auxiliary distribution functions are defined as:

$$\bar{\phi} = \phi - \frac{h}{2}\Omega_m, \quad \bar{\phi}^+ = \phi + \frac{h}{2}\Omega_m. \tag{15}$$

With these two auxiliary distribution functions $\bar{\phi}$ and $\bar{\phi}^+$, we apply Taylor expansion around the cell interface $\boldsymbol{x}_b$ and at time t_n, the Eq. (14) can be rewritten as:

$$\bar{\phi}(\boldsymbol{x}_b, \boldsymbol{\xi}, t_n + h) = \bar{\phi}^+(\boldsymbol{x}_b, \boldsymbol{\xi}, t_n) - h\boldsymbol{\xi}\cdot\nabla_{\boldsymbol{x}}\bar{\phi}^+(\boldsymbol{x}_b, \boldsymbol{\xi}, t_n). \tag{16}$$

Eq. (16) is totally explicit, $\bar{\phi}^+(\boldsymbol{x}_b, \boldsymbol{\xi}, t_n)$ and $\nabla_{\boldsymbol{x}}\bar{\phi}^+(\boldsymbol{x}, \boldsymbol{\xi}, t_n)$ can be expressed in terms of the values at the cell center by appropriate reconstruction method. The density and velocity at cell interface at half time step can be obtained from $\bar{\phi}(\boldsymbol{x}_b, \boldsymbol{\xi}, t_n + h)$, then the equilibrium function $\phi^{eq}(\boldsymbol{x}_b, \boldsymbol{\xi}, t_n + h)$ can be evaluated. Finally,

based on Eqs. (15) and (16), the original distribution function at cell interface $\boldsymbol{x}_b$ at time $t_n + h$ ca be obtained by:

$$\phi(\boldsymbol{x}_b, \boldsymbol{\xi}, t_n + h) = \frac{2\tau_\phi}{2\tau_\phi + h}\bar{\phi}(\boldsymbol{x}_b, \boldsymbol{\xi}, t_n + h) + \frac{h}{2\tau_\phi + h}\phi^{eq}(\boldsymbol{x}_b, \boldsymbol{\xi}, t_n + h) + \frac{\tau_\phi h}{2\tau_\phi + h}F_{ext}. \quad (17)$$

This original distribution function at half time step $\phi(\boldsymbol{x}_b, \boldsymbol{\xi}, t_n + h)$ can be used to evaluate the net flux $F_\phi(\boldsymbol{x}_b, \boldsymbol{\xi}, t_{n+1/2})$ in Eq. (13). Then the net flux can be used in Eq. (11) to update $\tilde{\phi}$. In the formulations above, we have one original distribution function ϕ and four auxiliary distribution functions $\tilde{\phi}$, $\tilde{\phi}^+$, $\bar{\phi}$ and $\bar{\phi}^+$. Conservative flow variables can be computed from any one of them, the most convenient way is to track the evolution of $\tilde{\phi}$. The hydrodynamic variable can be obtained as $\rho = \int \tilde{f} d\boldsymbol{\xi}$, $\rho \boldsymbol{u} = \int \boldsymbol{\xi} \tilde{f} d\boldsymbol{\xi} + \frac{\Delta t}{2}\rho \boldsymbol{a}$, $T = \int \tilde{g} d\boldsymbol{\xi}$.

It is worth noting that, as pointed out by Wang et al. [34], for DUGKS the non-uniform meshes can be easily employed without additional effort. Non-uniform meshes allow us to use finer mesh near the boundary to resolve the steep gradients of temperature and velocity especially near the cavity walls. Our 3D flow code has been parallelized using 2D domain decomposition in the y and z directions and MPI (Message Passing Interface) [32]. In the present study, the D3Q19 model is employed for the discretization of the particle velocity space,

$$\boldsymbol{\xi}_\alpha = \begin{cases} (0,0,0)c, & \alpha = 0, \\ (\pm 1,0,0)c,\ (0,\pm 1,0)c,\ (0,0,\pm 1)c, & \alpha = 1-6, \\ (\pm 1,\pm 1,0)c,\ (\pm 1,0\pm 1)c,\ (0\pm 1,\pm 1)c, & \alpha = 7-18, \end{cases} \quad (18)$$

where $c = \sqrt{3RT}$, and the corresponding weighting coefficient are $W_0 = 1/3, W_{1-6} = 1/18$ and $W_{7-18} = 1/36$.

2.3. Boundary treatment

For a wall-bounded thermal flow, it is crucial to implement the appropriate kinetic boundary conditions for the discrete distribution functions at the solid wall. One advantage of DUGKS is that we can apply boundary treatment right at the wall interface nodes which lie exactly on the solid wall. In DUGKS, the microscopic flux is calculated at the cell interface $\boldsymbol{x}_b$ at the half time step $t_n + h$. We need to apply the boundary condition for the distribution function $\bar{f}(\boldsymbol{x}_w, \boldsymbol{\xi}, t_n + h)$, where $\boldsymbol{x}_w$ is the location of the solid wall. It is important to point out that the boundary treatment should be consistent with the Chapman-Enskog approximation which is the basis for deriving the hydrodynamic equations. The incompressible Navier-Stokes equation can be recovered with the Chapman-Enskog expansion of the distribution function to the order of $\mathcal{O}(\tau_v)$. To be consistent with the Navier-Stokes equations, the boundary treatment should also retain the terms of the order $\mathcal{O}(\tau_v)$. For the fixed no-slip wall, we apply the bounce-back rule which assuming that the particle just reverses its velocity after hitting the wall:

$$f(\boldsymbol{x}_w, \boldsymbol{\xi}_\alpha, t_n + h) = f(\boldsymbol{x}_w, -\boldsymbol{\xi}_\alpha, t_n + h) + \mathcal{O}(\tau_v^2, Ma^3), \quad \boldsymbol{\xi}_\alpha \cdot \boldsymbol{n} > 0, \quad (19)$$

where $\boldsymbol{n}$ is the unit vector normal to the wall pointing to the fluid cell. The corresponding boundary condition for $\bar{f}(\boldsymbol{x}_w, \boldsymbol{\xi}, t_n + h)$ can be derived through Eq. (15). The 'bounce-back' expression above is widely used for the fixed no-slip wall, and it can be shown that it is fully consistent with the Chapman-Enskog analysis, namely, all terms of the order $\mathcal{O}(\tau_v)$ disappear due to the zero velocity on the wall.

However, the situation for the thermal boundary conditions is somewhat more complicated. There are two types of boundary conditions in our problem: adiabatic walls with zero heat flux and isothermal walls with a fixed temperature. For adiabatic walls, the Neumann boundary condition can be achieved by:

$$g(\boldsymbol{x}_w, \boldsymbol{\xi}_\alpha, t_n + h) = g(\boldsymbol{x}_w, -\boldsymbol{\xi}_\alpha, t_n + h) + 2\tau_c W_\alpha \xi_{a,i}\left(\frac{T_1}{T_2}\frac{T_w}{\rho_w}\frac{\partial \rho_w}{\partial x_i} - \frac{a_i T_w}{RT_2} - \frac{\partial T_w}{\partial x_i}\right) + \mathcal{O}(\tau_c^2, Ma^3), \quad \boldsymbol{\xi}_\alpha \cdot \boldsymbol{n} > 0. \quad (20)$$

where ρ, T, and temperature gradients in the tangential directions can be approximated by their respective values from the last time step and the temperature gradient in the wall normal direction is set to zero. The error introduced by the approximation is of the order $\mathcal{O}(\tau_c \Delta t)$, which is typically less than $\mathcal{O}(\Delta t^2)$ and thus is acceptable.

While for the isothermal walls, the distribution function leaving the wall should be constructed as:

$$g(\boldsymbol{x}_w, \boldsymbol{\xi}_\alpha, t_n + h) = -g(\boldsymbol{x}_w, -\boldsymbol{\xi}_\alpha, t_n + h) + 2W_\alpha T_w\left[1 + \tau_c\left(\frac{\partial u_j}{\partial x_j} - \frac{\xi_{a,i}\xi_{a,j}}{RT_2}\frac{\partial u_i}{\partial x_j}\right)\right] + \mathcal{O}(\tau_c^2, Ma^3), \quad \boldsymbol{\xi}_\alpha \cdot \boldsymbol{n} > 0. \quad (21)$$

where again the velocity at the last time step can be used to evaluate the velocity gradient. Most previous works neglected all $\mathcal{O}(\tau_c)$ terms for the thermal boundary conditions, this could result in inaccurate heat fluxes at the wall, especially in view of large variations of velocity and temperature near the wall and around the corners in our problem. The above Chapman-Enskog approximations of the thermal boundary conditions are derived in detail in Section Appendix A.

3. Results and discussions

This section will be divided into six parts. We first verify the code and compare our results with results from the literature. In order to elucidate the flow transition inside the vertical boundary layer, we simulate the natural convection flow at three different Rayleigh numbers: $Ra = 1.5 \times 10^9$, $Ra = 1.0 \times 10^{10}$, $Ra = 1.0 \times 10^{11}$. These Rayleigh numbers are beyond the critical Rayleigh number $Ra_{cr} = 3.19 \times 10^7$ for the current configuration [20]. Beyond the critical Rayleigh number, the flow becomes time-dependent and the first instability starts to appear in the detached regions (left upper corner and right bottom corner). The high Rayleigh numbers we used allow us to observe the second instability inside the boundary layers along the isothermal walls. The time-averaged isotherms and instantaneous fluctuation velocity contours are used to display the overall flow structures. The time traces of velocity and temperature inside the vertical boundary layer are used to illustrate the nature of fluctuations. Then we examine the averaged flow field at different vertical locations of the cavity. Statistics of fluctuation fields are also presented. Finally, The heat transfer rates at upstream and downstream in the thermal boundary layer are analyzed.

3.1. Code verification and computational cases

Before considering high Rayleigh number cases, the three-dimensional code is tested at $Ra = 1.0 \times 10^7$ by comparing with three-dimensional spectral results of Tric et al. [17]. We apply non-uniform grids in all three directions to guarantee that the steep gradient near the wall can be resolved. Table 1 summarizes the results of time-averaged overall Nusselt number $\overline{Nu}_o$ at hot wall and maximum flow velocities in three directions at $Ra = 1.0 \times 10^7$. It

Table 1
Comparison of our simulation results with the reference results for a cubical cavity at $Ra = 1.0 \times 10^7$.

$Ra = 10^7$	Spatial resolution	$\overline{Nu}_o$	$\hat{u}_{max}$	$\hat{v}_{max}$	$\hat{w}_{max}$
Present	$128 \times 128 \times 128$	16.234	0.2863	0.1428	0.0308
Tric et al. [17]	$81 \times 81 \times 81$	16.342	0.2882	0.1440	0.0313
Rel. error (%)		0.661	0.601	0.379	0.158

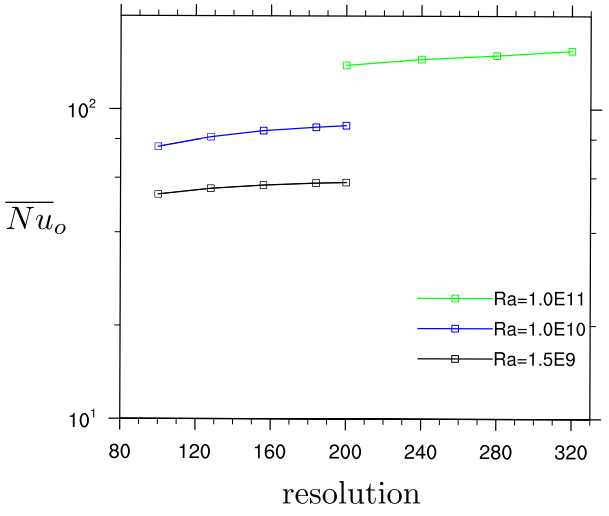

Fig. 2. Time-averaged overall Nusselt number at hot wall as a function of resolution for three Rayleigh numbers: $Ra = 1.5 \times 10^9$, $Ra = 1.0 \times 10^{10}$, $Ra = 1.0 \times 10^{11}$.

can be observed that the present results agree well with the reference results. The largest relative error $\frac{|\Delta \hat{u}_{max}|}{u_0}$ is less than 1%. More code verification simulation cases are shown in Appendix A.

Regarding the numerical setup, the entire cubic cavity constitutes the full computational domain, Table 2 tabulates the stretched meshes and the non-dimensional time step size of three cases. In order to resolve steep gradient of velocity and temperature near the wall, non-uniform meshes are introduced in three directions. For a set of stretched meshes with N grid points in each direction, the location of the cell interface $x_b(i)$ is given by:

$$x_b(i) = \frac{1}{2}\left[1 + \frac{\tanh[S(i/N - 0.5)]}{\tanh(S/2)}\right], \quad i = 0, 1, 2, ..., N, \tag{22}$$

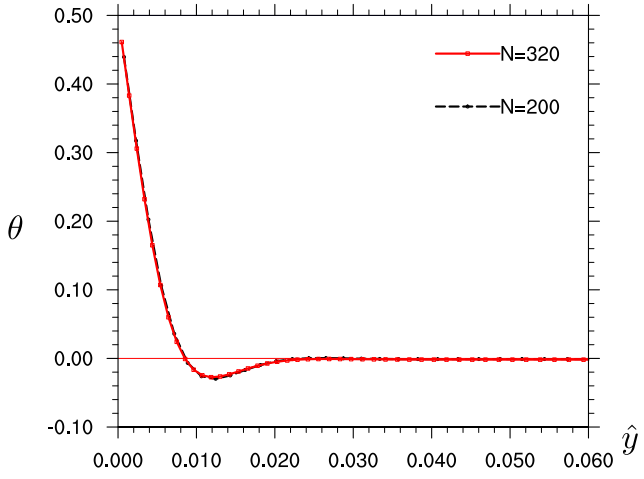

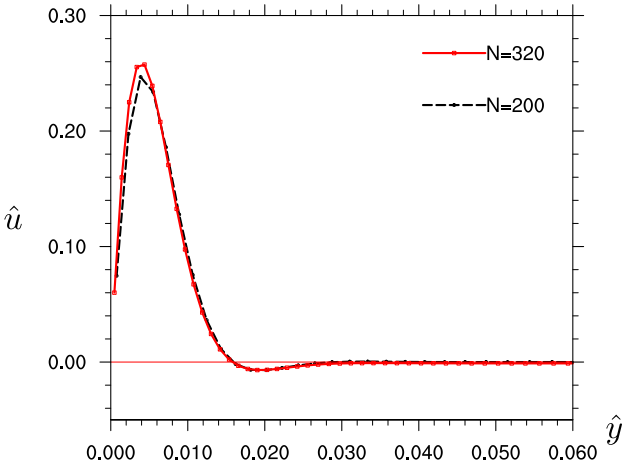

Fig. 3. The temperature θ and the vertical velocity $\hat{u}$ profiles at the mid-plane $z = 0.5h$ and mid height $x = 0.5h$ at $Ra = 1.0 \times 10^{10}$ with the resolutions $N = 200$ (I) and $N = 320$ (II).

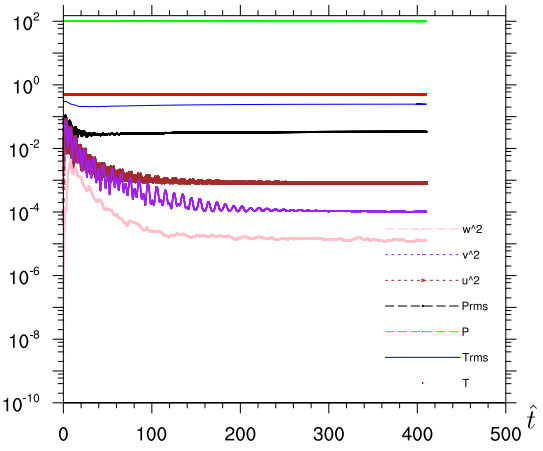

Fig. 4. Flow monitor for $Ra = 1.5 \times 10^9$.

where S is the parameter used to alter the degree of non-uniformity, S is set to be 3 for all simulation cases. Then the location of the cell center can be obtained by $x(i) = [x_b(i) + x_b(i+1)]/2$. To guarantee the resolution is fine enough to resolve the steep gradient near the wall, we use two-dimensional convection flow to perform the convergence study. As claimed by Trias et al. [23], two-dimensional natural convection in a square cavity is a good approximation of the flow at the mid-plane of the three-dimensional cubical cavity. Fig. 2 displays the overall Nusselt number at the hot wall as a function of resolution. In each case, the time-averaged overall Nusselt number converges to a certain value with the increase of the resolution. As the three-dimensional simulations require large computational resources, the resolutions we employ represent a reasonable compromise between accuracy and computational cost. In particular, the convergence for the $Ra = 1.0 \times 10^{11}$ case is not fully achieved. Besides, an increased spatial resolution will result in a smaller time step due to the CFL condition $\Delta t = CFL\frac{\Delta x_{min}}{\xi_{max}}$, this will further increase the computational cost. Even though the resolution we used is a compromise, there are over 10 nodes insides the temperature and the velocity boundary layers. This satisfies the requirement of grid resolution for capturing the universal structure of the boundary layer according to Grötzbach [36] but not yet reaches the standard proposed by Shishkina et al. [37], both for the Rayleigh-Bénard setting. Ac-

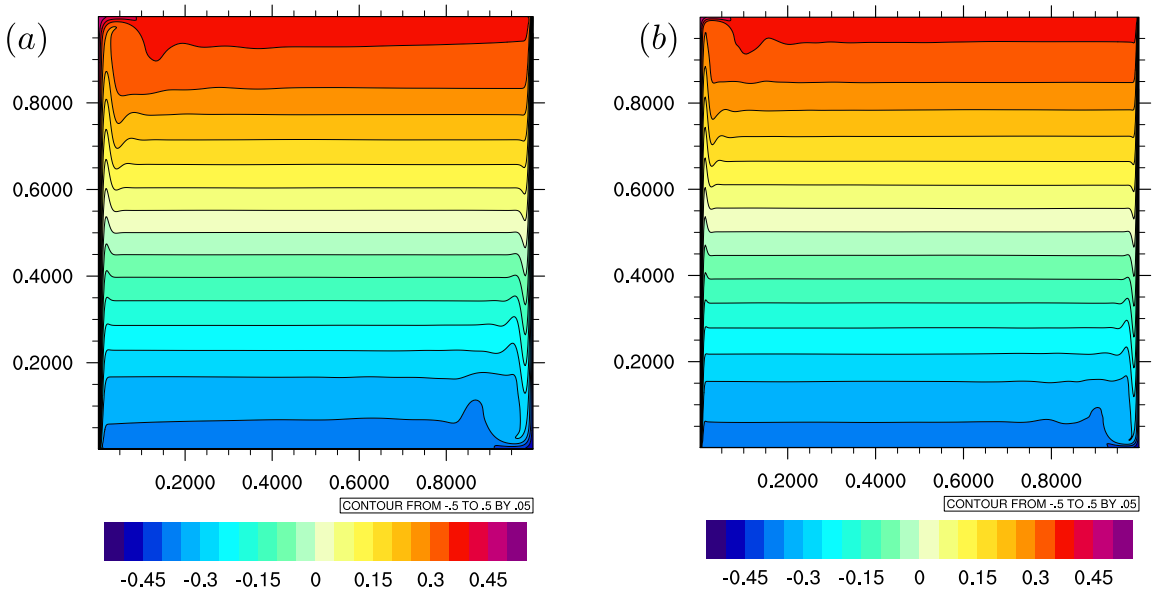

Fig. 5. Time-averaged temperature field $\tilde{\theta}$ for: $(a) Ra = 1.5 \times 10^9$; $(b) Ra = 1.0 \times 10^{10}$.

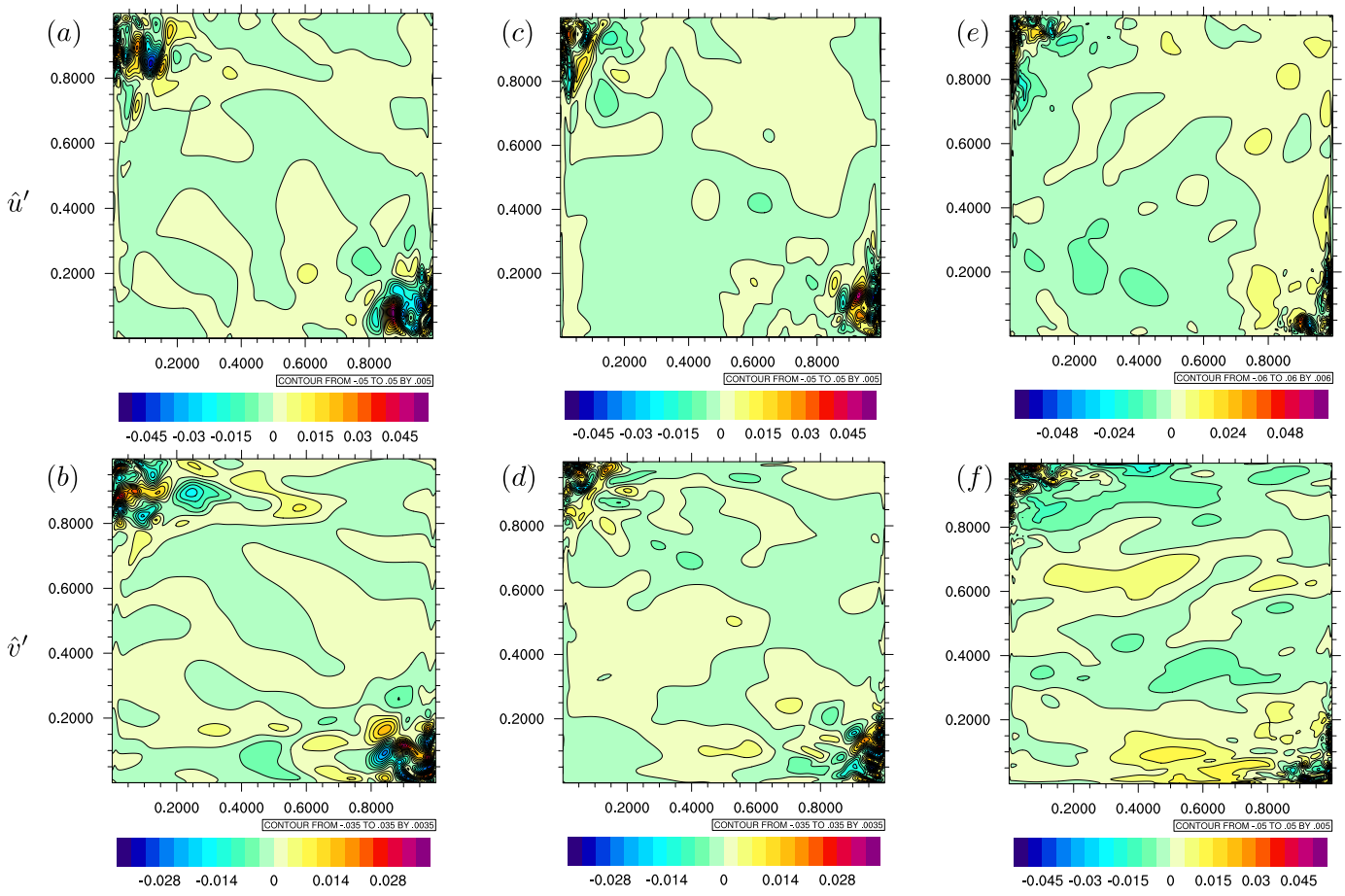

Fig. 6. Contour plot of instantaneous fluctuating vertical velocity $\hat{u}' = \frac{u-\overline{u}}{u_0}$ (top) and horizontal velocity $\hat{v}' = \frac{v-\overline{v}}{u_0}$ (bottom) for three Rayleigh numbers: $(a)(b)$ $Ra = 1.5 \times 10^9$, $(c)(d)$ $Ra = 1.0 \times 10^{10}$, $(e)(f)$ $Ra = 1.0 \times 10^{11}$.

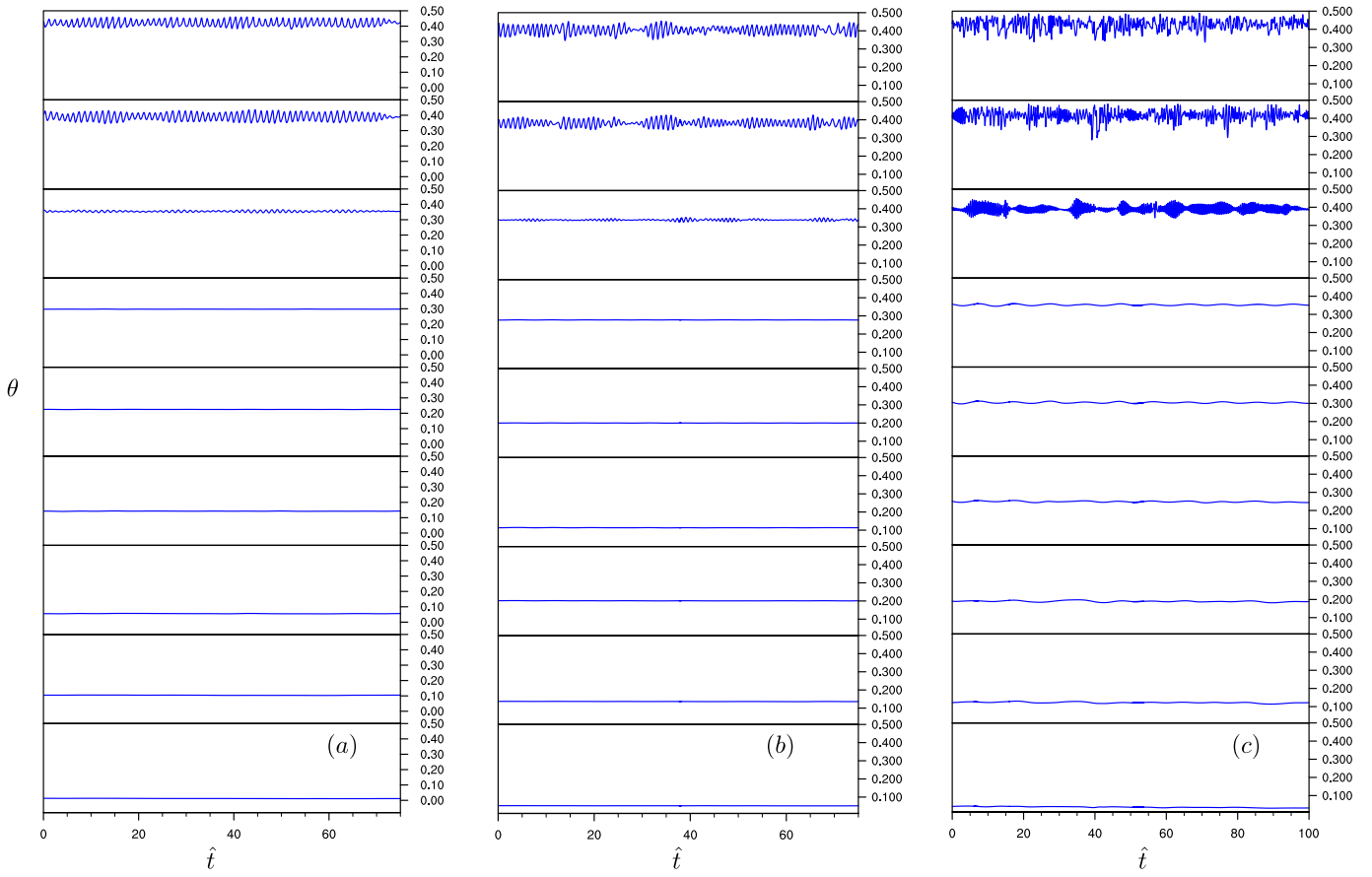

Fig. 7. Time traces of temperature at monitoring points in 9 vertical locations, $x/h = 0.1$ to 0.9 with increment of 0.1, at (a) $Ra = 1.5 \times 10^9$, (b) $Ra = 1.0 \times 10^{10}$, (c) $Ra = 1.0 \times 10^{11}$.

cording to the scaling of laminar thermal boundary layer thickness, we propose that the value of $(Ra^{1/4} \cdot \Delta x_{\min}/l)$ should be less than a given threshold. Table 2 tabulates the value $Ra^{1/4} \cdot \Delta x_{\min}/l$ for each case. Since the case of $Ra = 1.5 \times 10^9$ is shown to be well resolved, we could use the condition of $Ra^{1/4} \cdot \Delta x_{\min}/l \leq 0.30$ as the resolution requirement for $Ra = 1.0 \times 10^{10}$ and $Ra = 1.0 \times 10^{11}$ cases. Two resolutions ($N = 200$ and $N = 320$) are used to simulate the $Ra = 1.0 \times 10^{10}$ case for some additional grid sensitivity study. Fig. 3 shows the time-averaged temperature θ and vertical velocity $\hat{u}$ profiles for the case $Ra = 1.0 \times 10^{10}$ with two resolutions $N = 200$ and 320. The result shows that the boundary layer thickness is nicely captured by both resolutions. In the following sections, the results of the case $Ra = 1.0 \times 10^{10}$ are obtained with the $N = 200$ resolution unless otherwise mentioned. The resolution of the highest Rayleigh number case ($Ra = 1.0 \times 10^{11}$) does not meet the requirement, and as such the accuracy of results for this case should be taken with caution.

3.2. Overall flow structures

Before a detailed analysis of the boundary layer, we first present the overall structures of the flow. All statistics used in the following analysis are obtained after the flow reaches the quasi-steady or statistically stationary stage. The development of the flow is tracked by a few spatially-averaged flow monitors ($\overline{\hat{u}^2}, \overline{\hat{v}^2}, \overline{\hat{w}^2}, \overline{p}, \overline{p_{rms}}, \overline{T}, \overline{T_{rms}}$). For example, Fig. 4 shows the spatial-averaged flow statistics for the case $Ra = 1.5 \times 10^9$, as a function of time. This shows that different quantities took different times to reach the stationary stage. After $\hat{t} = 300$, all the monitoring statistics reach the stationary stage. The statistics used for analysis are averaged over 75 eddy turn-over times after $\hat{t} = 300$. The code was run on the National Center for Atmospheric Research's (NCAR-Wyoming) Supercomputer, known as Cheyenne, equipped with 2.3-GHz Intel Xeon E5-2697V4 processors. The computational domain are decomposed in the y and z direction, 400 processors are employed for the case $Ra = 1.5 \times 10^9$. The wall clock time per step is $9.56 \times 10^{-2}s$, and it takes 9.5×10^6 time steps to reach $\hat{t} \approx 300$. For the case $Ra = 1.0 \times 10^{10}$ with $N = 200$ resolution, the wall clock time per step is the same with the case $Ra = 1.5 \times 10^9$. For the case $Ra = 1.0 \times 10^{11}$, 1024 processors are used and the wall clock time per step is $1.83 \times 10^{-1}s$, and 1.5×10^7 time steps are needed to reach $\hat{t} \approx 300$. Fig. 5 shows the time-averaged temperature field $\bar{\theta}$ at the mid-plane ($z = 0.5$) of the cavity, when the flow reaches the statistically stationary stage. Generally speaking, the time-averaged isotherms is asymmetric about the cavity center, extremely thin boundary layers are developed along the isothermal wall. With the increase of the Rayleigh number, the boundary thickness becomes smaller.

For these high Rayleigh numbers, the flow is unsteady and fluctuates in time. Fig. 6 shows the instantaneous velocity fluctuation field $\hat{\boldsymbol{u}}' = \frac{\boldsymbol{u}-\bar{\boldsymbol{u}}}{u_0}$ at three Rayleigh numbers after flow reaches the stationary stage. The cavity center is no longer steady and now fluctuates in time. The vortices are generated at the downstream of the boundary layers and are shed from the upper corner on the heated wall. The size of the vortices becomes smaller with the increase of the Rayleigh numbers.

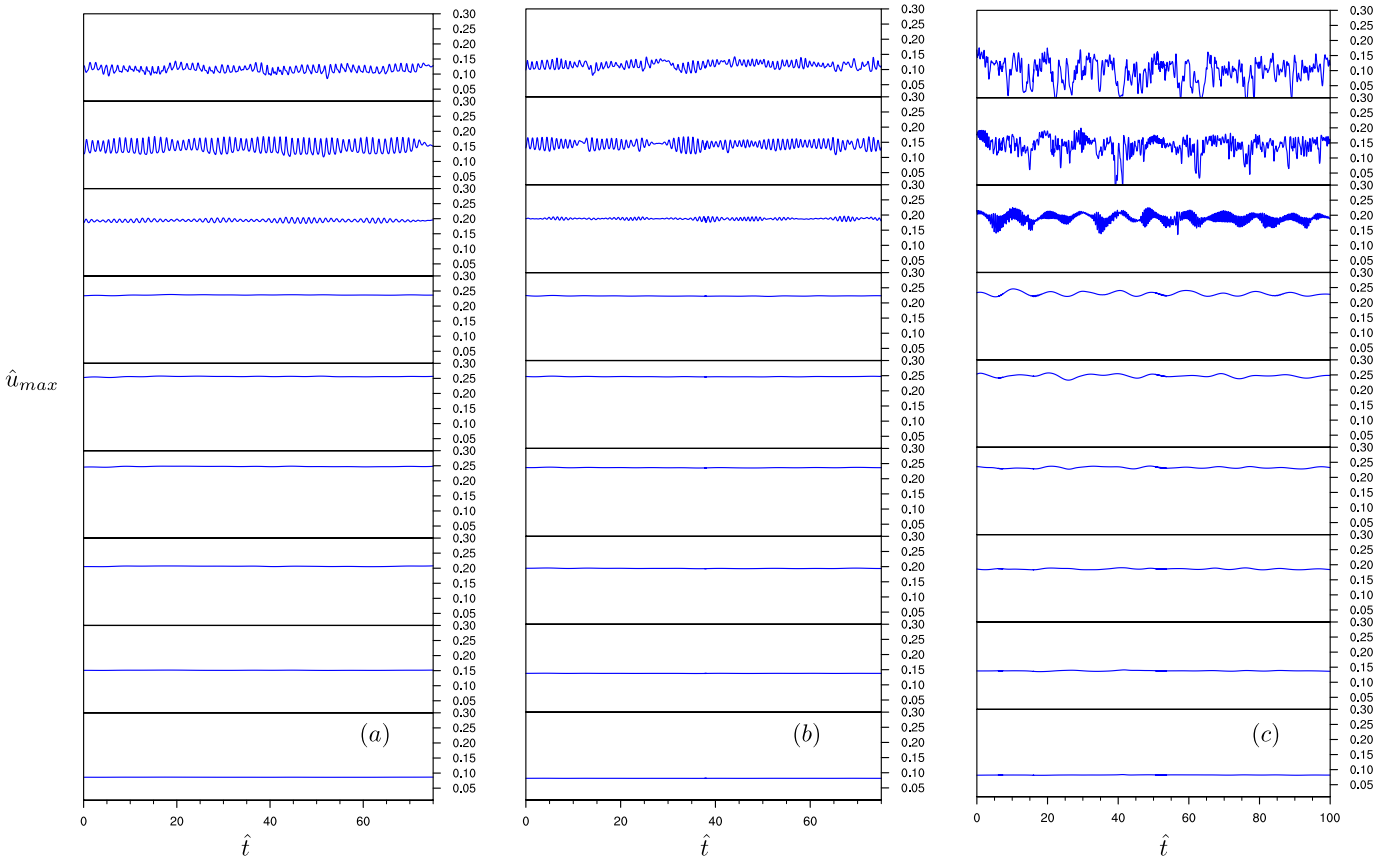

Fig. 8. Time trace of velocity at monitoring points $x = 0.1h \sim x = 0.9h$ at (a) $Ra = 1.5 \times 10^9$, (b) $Ra = 1.0 \times 10^{10}$, (c) $Ra = 1.0 \times 10^{11}$.

3.3. Time traces of the temperature and velocity

Driven by the buoyancy force, the flow gradually develops from laminar to turbulent flow along the vertical boundary layer adjacent to two isothermal walls. The upstream part is usually laminar, and up to a point after which the flow becomes turbulent. As the velocity signals of laminar and turbulent flow are evidentially different, we track the time traces of the temperature and velocity inside the vertical boundary layer along the hot wall. Firstly, we need to ensure the monitoring points are located inside the boundary layer. Based on the time-averaged temperature and velocity profile at nine different vertical locations ($x = 0.1h - 0.9h$), for temperature evolution, a set of monitoring points are chosen at the mid-plane ($z = 0.5h$), as a y location where $T(x, y, z = 0.5h) = \frac{T_h + T_\infty(x, z=0.5h)}{2}$, $T_\infty(x, z = 0.5h)$ is the temperature outside the boundary layer at the given x level. Due to temperature stratification in the core region, $T_\infty(x)$ changes with the vertical location x. For the velocity trace, the monitoring points are at the location where $u = u_{\max}$ at that height. In this way, we can guarantee that all the monitoring points are located inside the boundary layer.

The time traces of temperature and velocity at 9 monitoring points for each of the three different Rayleigh numbers are shown in Figs. 7 and 8. All the time traces are obtained after the flow reaches the stationary stage. From the plots, we can observe that the upstream region with time-independent behavior is from $x = 0$ to $x = 0.7h$ for the cases $Ra = 1.5 \times 10^9$ and 1.0×10^{10}; but for $Ra = 1.0 \times 10^{11}$ the upstream region is reduced to the region from $x = 0$ to $x = 0.6h$, roughly speaking. For the cases $Ra = 1.5 \times 10^9$ and 1.0×10^{10} the flow is laminar and steady in the upstream region, while for $Ra = 1.0 \times 10^{11}$ it is laminar and unsteady. In contrast, the temperature and velocity of the downstream fluctuate over time, and the fluctuation amplitude and the frequency range increase with Ra. Similar fluctuation behaviors of the velocity and temperature in the downstream region are reported by Xin and Quéré [38] for vertical boundary layer at the hot wall of a two-dimensional differentially heated cavity of aspect ratio at 4. Based on the time traces of $\hat{u}$ velocity for $Ra = 1.0 \times 10^{10}$ and $Ra = 1.0 \times 10^{11}$, Table 3 tabulates the partition of energy in the mean and in the fluctuating motion. The ratio is negligible in the upstream for both Rayleigh numbers, while in the downstream region more kinetic energy participates in fluctuation. Especially for the Rayleigh number $Ra = 1.0 \times 10^{11}$, the relative partition of fluctuation energy at the height $x = 0.9h$ is more than 14%.

To investigate the fluctuation frequency of the velocity and temperature insides boundary layer, we provide the spectra of velocity fluctuation $\frac{u'(\hat{f})}{u_0}(u' = u - \bar{u})$ and temperature fluctuation $\theta'(\hat{f})$ in the Figs. 9 and 10. The spectra are obtained from time trace signals spanning over a time duration of approximately $70h/u_0$ for the two lower Rayleigh number cases, and $100h/u_0$ for the $Ra = 1.0 \times 10^{11}$. Three locations are selected to show the transition of the velocity: $x = 0.2h$ near the starting point of the upstream, $x = 0.5h$ at the mid-height, and $x = 0.9h$ at the downstream. As the temperature time trace is similar to the velocity time trace, we only provide the spectra of temperature $\theta'(\hat{f})$ for the location $x = 0.9h$. For two locations at the upstream, the spectral magnitudes are relatively small and the velocity spectra are dominated by low-frequency oscillations. It is also noted that the magnitude of the spectra for the location $x = 0.2h$ is very small, especially for the cases $Ra = 1.5 \times 10^9$ and $Ra = 1.0 \times 10^{10}$, the oscillations in the upstream are negligible. While for the upstream, energy concentrates near the mean mode ($\hat{f} = 0$), the downstream velocity fluctuation spreads out into the high-frequency region. As pointed out by Janssen and

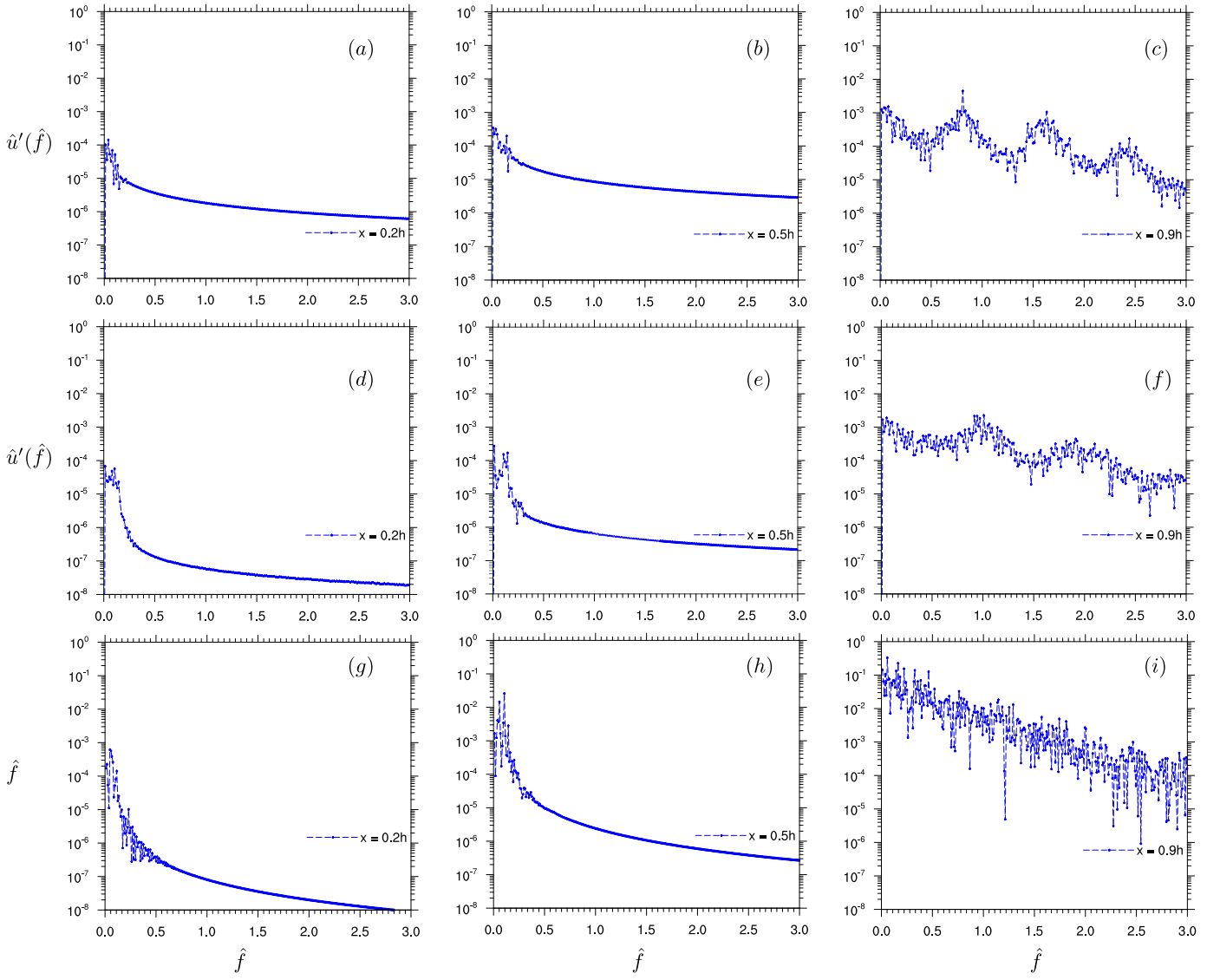

Fig. 9. Spectra of velocity fluctuation $\hat{u}'(\hat{f})$ at three monitoring points. From top to bottom: (a) (b) (c) for $Ra = 1.5 \times 10^9$; (d) (e) (f) for $Ra = 1.0 \times 10^{10}$; (g) (h) (i) for $Ra = 1.0 \times 10^{11}$.

Table 2
The non-uniform meshes used for the simulations.

Ra	Spatial resolution	$\frac{\Delta x_{min}}{l}$	$Ra^{\frac{1}{4}} \cdot \frac{\Delta x_{min}}{l}$	$\frac{\Delta x_{max}}{\Delta x_{min}}$	$\frac{u_0 \Delta t}{h}$
1.5×10^9	$200 \times 200 \times 200$	1.52×10^{-3}	0.299	5.4587	3.1623×10^{-5}
1.0×10^{10}[I]	$200 \times 200 \times 200$	1.52×10^{-3}	0.481	5.4587	3.1623×10^{-5}
1.0×10^{10}[II]	$320 \times 320 \times 320$	9.44×10^{-4}	0.299	5.4869	1.9764×10^{-5}
1.0×10^{11}	$320 \times 320 \times 320$	9.44×10^{-4}	0.531	5.4869	1.9764×10^{-5}

Table 3
Relative partition of energy $\frac{\overline{\hat{u}'^2}}{\overline{\hat{u}^2}}$ in the mean and in the fluctuation (%).

Ra	$0.1h$	$0.2h$	$0.3h$	$0.4h$	$0.5h$	$0.6h$	$0.7h$	$0.8h$	$0.9h$
1.0×10^{10}	1.1088e-4	2.0790e-4	8.6940e-4	7.2612e-4	5.0661e-4	7.1279e-4	0.0286	0.7535	0.9667
1.0×10^{11}	0.0022	0.0053	0.0087	0.0123	0.0403	0.0689	0.6112	3.9789	14.1829

Henkes [11], the time-periodic flow is characterized by the phenomenon that the power spectra of the velocity show a peak at a single frequency; and the quasi-periodic flow shows at lease two spikes (two fundamental frequencies and the linear combination of the fundamental spike) at two frequencies in their power spectra; while turbulent flow has a broadband power spectra. The peak frequency at the $x = 0.9h$ of the case $Ra = 1.5 \times 10^9$ is around $\hat{f} = 0.8$, this agrees well with the two-dimensional results of the Janssen and Henkes [11]. They obtain the peak frequency around $\hat{f} = 0.8$ at $Ra = 7.5 \times 10^8$ from the temperature time trace at the same height. This non-dimensional peak frequency of $\hat{f} = 0.8$ compares well with the period of about 1.21 observed in time trace of the temperature and the velocity as shown in Figs. 7(a) and 8(a). From the spectra at the location $x = 0.9h$ for three Rayleigh num-

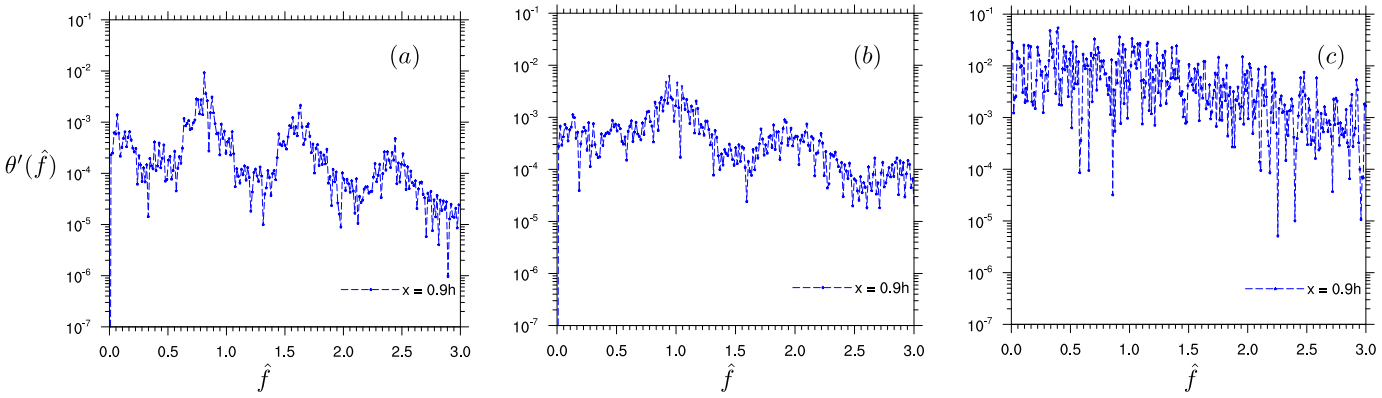

Fig. 10. Spectra of temperature fluctuation $\theta'(\hat{f})$ at monitoring points $x = 0.9h$. For (a) $Ra = 1.5 \times 10^9$, (b) $Ra = 1.0 \times 10^{10}$, (c) $Ra = 1.0 \times 10^{11}$.

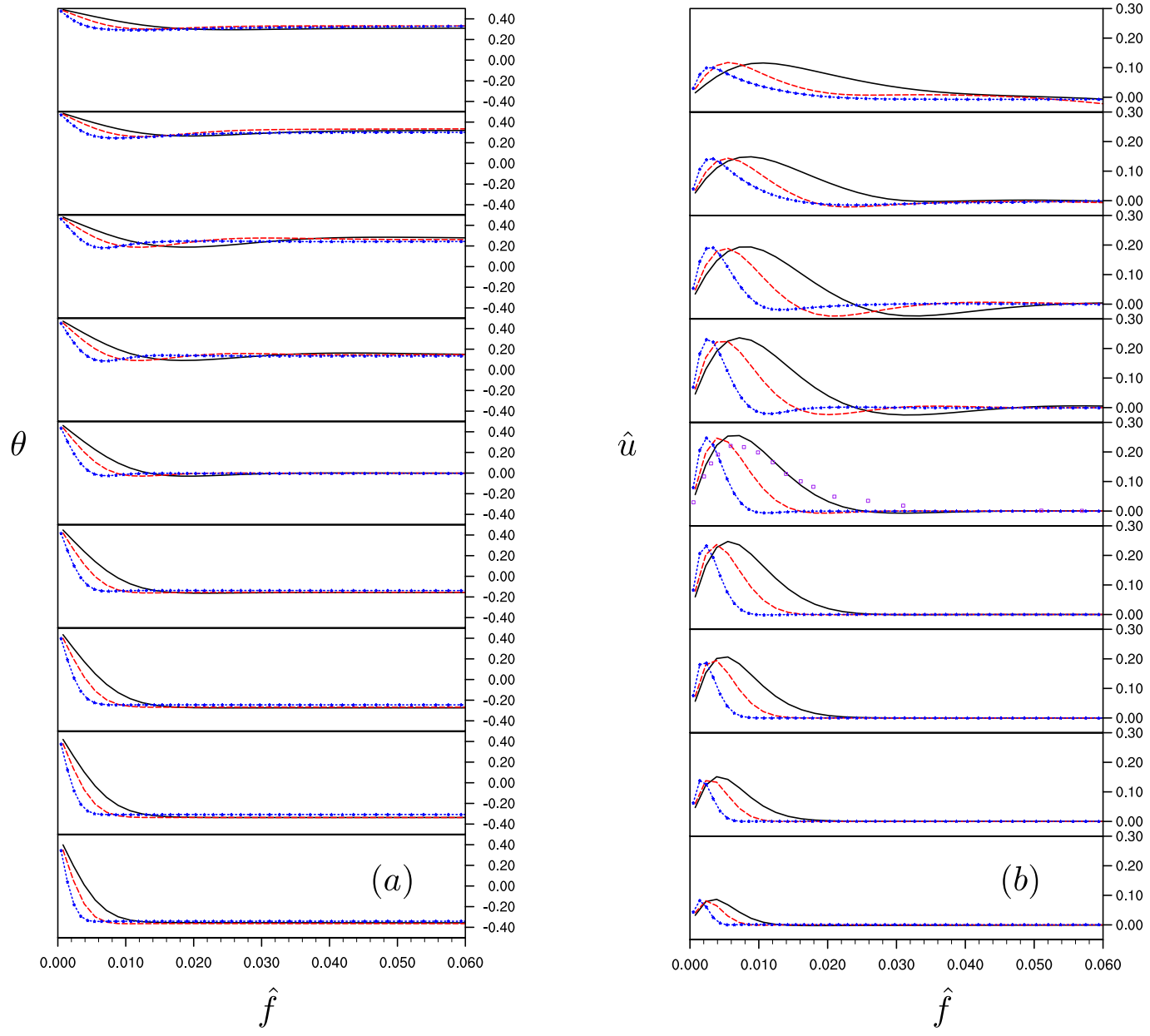

Fig. 11. (*a*) Time-averaged temperature, (*b*) Vertical velocity profiles in the mid-plane $z = 0.5h$ at $x = 0.1h \sim x = 0.9h$, $Ra = 1.5 \times 10^9$ (black line), $Ra = 1.0 \times 10^{10}$ (red dash line), $Ra = 1.0 \times 10^{11}$ (blue dash line). The purple squares in (*b*) are experimental data of Salat et al. [6] at $Ra = 1.5 \times 10^9$. (For interpretation of the references to color in this figure legend, the reader is referred to the web version of this article.)

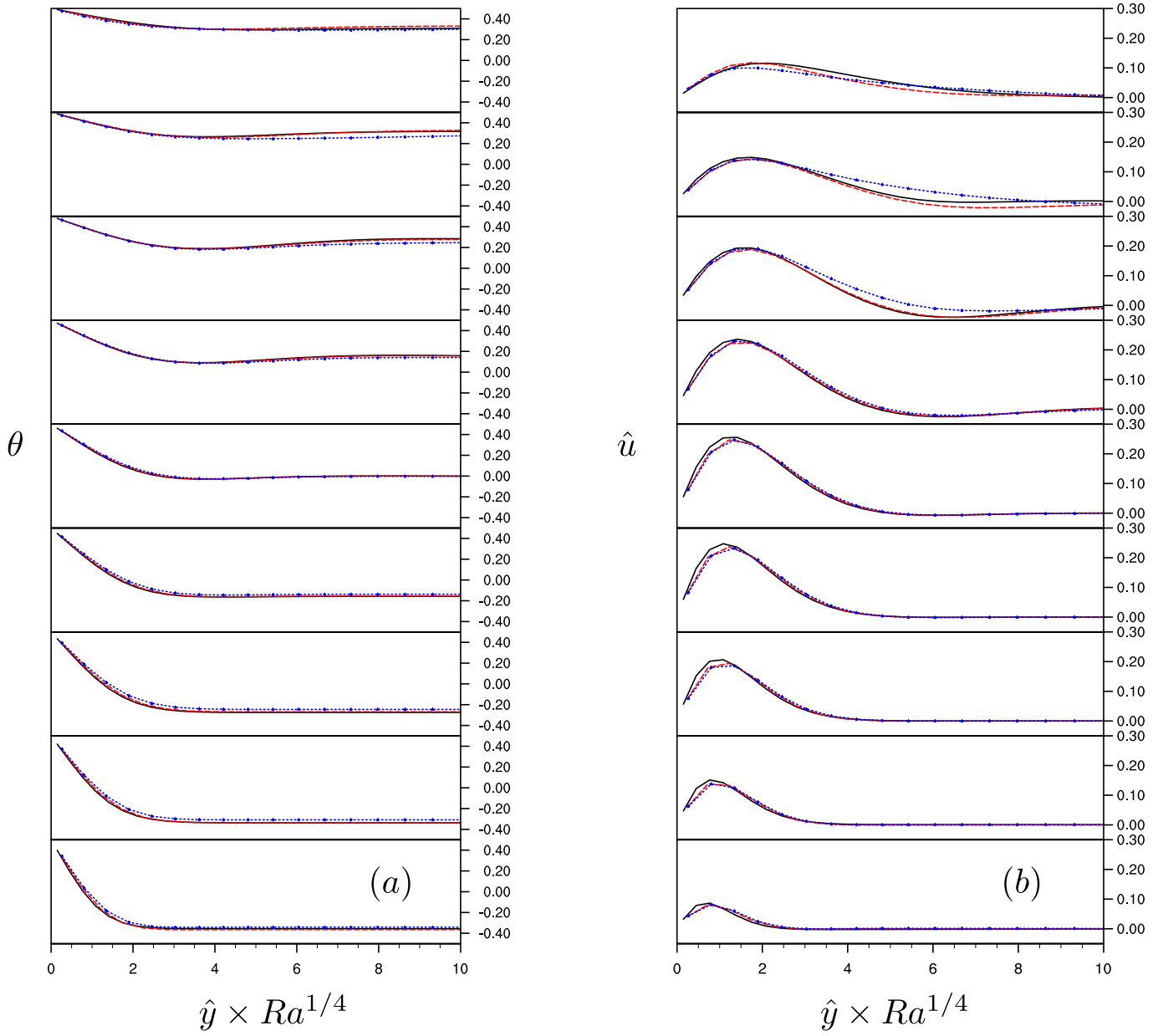

Fig. 12. (*a*) Temperature profiles with abscissa scaled by $Ra^{1/4}$, and (*b*) vertical velocity profiles with abscissa scaled by $Ra^{1/4}$ in the mid-plane $z = 0.5h$ at $x = 0.1h \sim x = 0.9h$, $Ra = 1.5 \times 10^9$ (black line), $Ra = 1.0 \times 10^{10}$ (red dash line), $Ra = 1.0 \times 10^{11}$ (blue dash line). (For interpretation of the references to color in this figure legend, the reader is referred to the web version of this article.)

bers, we can observe that the two lower *Ra* cases are characterized by spectra with spikes at two fundamental frequencies plus spikes at linear combinations of the fundamental frequencies which indicate the flow is quasi-periodic; and the case $Ra = 1.0 \times 10^{11}$ has broadband spectra instead of the specific peaks at a certain frequency. The spectra of the location $x = 0.5h$ for $Ra = 1.0 \times 10^{11}$ is characterized by a single spike at low-frequency and this phenomenon shows the flow in this location is periodic. In the case of $Ra = 1.0 \times 10^{11}$, the frequency spectrum of the velocity fluctuations Fig. 9(i) appears to decay exponentially, similar to the dissipation range of high-Reynolds number turbulence, the frequency spectrum of the temperature fluctuations Fig. 10(c) exhibits a more complex shape implying perhaps different structures of temperature fluctuations compared to the velocity fluctuations. From the analysis above we can observe that insides the boundary layer, the upstream part remains laminar until when the local flow starts to shed vortices to produce quasi-periodic or turbulent flow downstream. With the increase of the Rayleigh number, the downstream of the boundary layer becomes turbulent eventually.

3.4. Averaged flow field

The time-averaged temperature and vertical velocity profiles at the mid-plane are displayed in Fig. 11. As shown in Fig. 11(*a*) and (*b*), both the thicknesses of velocity and thermal boundary increase with increasing distance from the starting location of the boundary layer. At the same height, with the increase of *Ra*, the thickness of boundary layer becomes smaller and the vertical velocity peak moves towards the wall. And at mid-height $x = 0.5h$, our results agree well with the experimental results of Salat et al. [6]. Corresponding to the thinner boundary layer, the temperature gradient near the boundary becomes larger at higher *Ra*. Fig. 12(*a*)

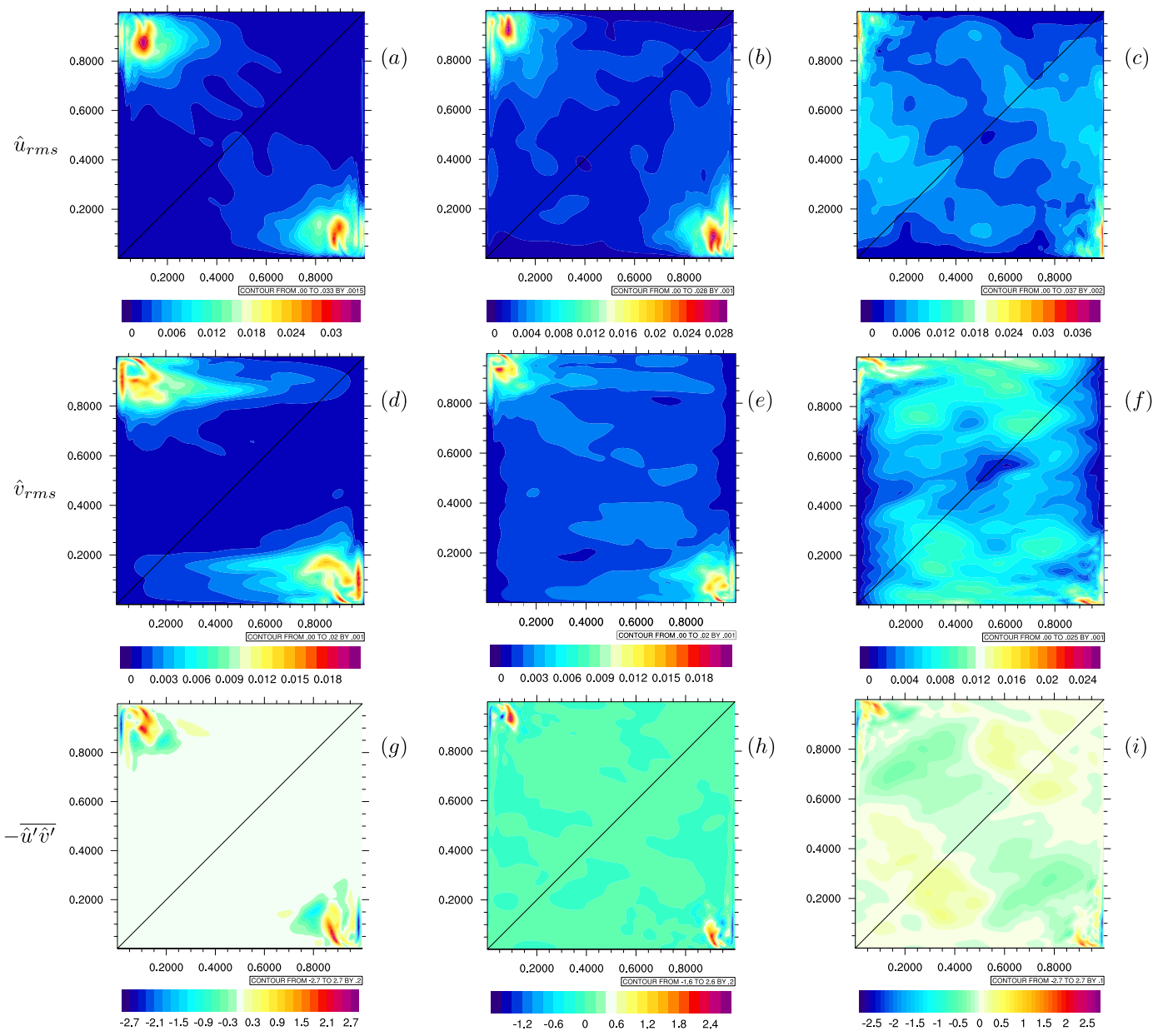

Fig. 13. Averaged turbulent fluctuation statistics from top to bottom: $\hat{u}_{rms}$, $\hat{v}_{rms}$, $-\overline{\hat{u}'\hat{v}'} \times 10^4$. Left: $Ra = 1.5 \times 10^9$, middle: $Ra = 1.0 \times 10^{10}$, right: $Ra = 1.0 \times 10^{11}$.

and (b) show the time averaged temperature and velocity profiles with the abscissa scaled by the laminar scaling factor $Ra^{1/4}$ [1]. For the upstream part ($x = 0$ to $x = 0.7h$), almost identical temperature and velocity profiles are obtained after the scaling. Similar results are reported by Trias et al. [23]. Discrepancies occur only in downstream part, and the differences start to appear at the point where temperature and velocity start to fluctuate and reach its maximum around $x = 0.8h$. This observation again confirms that for the Ra range being studied, the major part ($x = 0 - 0.7h$) of the vertical boundary layer is still laminar, and the transition from the laminar to time-dependent turbulent flow happens around the height $x = 0.7h$.

3.5. Turbulent fluctuation statistics

Turbulent fluctuation statistics ($\hat{u}_{rms}$, $\hat{v}_{rms}$, $-\overline{\hat{u}'\hat{v}'}$) of the mid-plane $z = 0.5h$ are displayed in Fig. 13. As the flow is dominated by vertical velocity $\hat{u}$ and horizontal velocity $\hat{v}$, we measure the Reynolds stress $-\overline{\hat{u}'\hat{v}'}$. It should be noted that the velocity $\hat{w}$ in the lateral direction is almost one order of magnitude lower than $\hat{u}$, $\hat{v}$. For $Ra = 1.5 \times 10^9$ and 1.0×10^{10}, the active turbulence is located at left top and bottom right corners indicating regions for the first occurrence of turbulence. For these two Rayleigh numbers, the turbulent fluctuation statistics start to be significant at the height $x = 0.7h$. Outside the boundary layer, all turbulent statistics are almost zero. For $Ra = 1.0 \times 10^{11}$, the distribution of turbulent fluctuation statistics are more complex than the lower Ra cases. Small fluctuations exist in the core region, the high value region of turbulent fluctuation statistics still concentrates in the downstream corners. And the transition point moves upstream, the significant turbulent fluctuations appear around the height $x = 0.65h$. From this local distribution of the turbulence statistics, we can clearly observe that for the lower two Ra cases, the core region and upstream of the vertical boundary are still laminar, the turbulent fluctuations are

Table 4
Time-averaged mean Nusselt number and $Nu - Ra$ correlations.

Ra	$\overline{Nu}_o$	$\frac{\overline{Nu}_o}{Ra^{1/4}}$	$\frac{\overline{Nu}_o}{Ra^{1/3}}$	$\overline{Nu}_{up}$	$\frac{\overline{Nu}_{up}}{Ra^{1/4}}$	$\overline{Nu}_{down}$	$\frac{\overline{Nu}_{down}}{Ra^{1/4}}$	$\frac{\overline{Nu}_{down}}{Ra^{1/3}}$
1.5×10^9	58.08	0.2953	0.0508	73.30	0.3725	22.65	0.1151	0.0198
Fusegi et al. [18]	63.07	0.3205	0.0551					
Wang et al. [22] (1.0×10^9)	52.08	0.2929	0.0521					
1.0×10^{10}[I]	89.29	0.2824	0.0414	112.1	0.3545	36.05	0.1140	0.0167
1.0×10^{10}[II]	94.21	0.2979	0.0437	134.1	0.4240	35.91	0.1135	0.0167
Fusegi et al. [18]	107.7	0.3406	0.0500					
Wang et al. [22]	89.2	0.2821	0.0414					
1.0×10^{11}	154.6	0.2750	0.0333	217.6	0.3870	62.59	0.1113	0.0135

only significant in the downstream corners. It is suggested that for $Ra = 1.5 \times 10^9$ and 1.0×10^{10}, the flow is only weakly turbulent as pointed out by Salat et al. [6]. For $Ra = 1.0 \times 10^{11}$, the fluctuations exist in the whole domain, but the high value of turbulent statistics concentrate in the downstream corners, and the flow becomes turbulent. To the authors' knowledge, $Ra = 1.0 \times 10^{11}$ is the highest Ra reported for three dimensional natural convection in a differentially heated cubical cavity with adiabatic horizontal walls.

3.6. Heat transfer

From the averaged flow field we can clearly observe that the thickness of the boundary layer becomes smaller with the increase of Ra, and thinner boundary layer leads to larger temperature gradient near the boundary. Steep temperature gradient intensifies the heat transfer near the boundary. Mean Nusselt number Nu_o at hot wall is defined as:

$$Nu_o = \frac{1}{h\Delta T}\int_0^h\int_0^h \frac{\partial T(x,z)}{\partial y}\bigg|_{y=0} dxdz = \int_0^1\int_0^1 \frac{\partial \theta(\hat{x},\hat{z})}{\partial \hat{y}}\bigg|_{\hat{y}=0} d\hat{x}d\hat{z} \tag{23}$$

Table 4 shows time-averaged mean Nusselt number $\overline{Nu}_o$ at the hot wall for three different Rayleigh numbers. Our results are in excellent agreement with Wang et al. [22]. It should be noted that the $Nu - Ra$ correlation reported by Wang et al. [22] was given in two Ra ranges respectively ($Nu_o = 0.127Ra^{0.3052}$ for $10^3 \le Ra \le 10^7$; $Nu_o = 0.3408Ra^{0.241}$ for $10^7 \le Ra \le 10^{10}$), while Fusegi et al. [18] proposed Rayleigh-Nusselt dependence in one correlation ($Nu_o = 0.163Ra^{0.282}$ for $10^3 \le Ra \le 10^{10}$). And the resolution used by Wang et al. [22] is relatively finer than Fusegi et al. [18]. In the current study, we evaluate the time-averaged overall Nusselt number for the Rayleigh range $10^3 \le Ra \le 10^{11}$ as shown in Fig. 14. In the steady regime, our results agree well with both reference fitting. In the unsteady flow regime, the thermal boundary layer becomes thinner with the increase of the Rayleigh number. The maximum number of grid points used by Fusegi et al. [18] is $122 \times 62 \times 62$. Wang et al. [22] employed 200^3 non-uniform meshes for $Ra = 10^{10}$. In the current study, the resolution we used for the highest Rayleigh number ($Ra = 1.0 \times 10^{11}$) may not be adequate, as such the average Nu number for this case is not shown in the figure.

From Table 4, we can observe that the $Nu - Ra$ correlation for mean Nusselt number at the hot wall is much closer to laminar scaling factor $Ra^{1/4}$ than turbulent scaling $Ra^{1/3}$ expected from natural convection over an unbounded flat plate [1]. When the convection flow reaches the stationary stage, due to temperature stratification, the cold fluid is distributed in the bottom while hot fluid in the top, thus the temperature gradient in the upstream of the vertical boundary would be larger than in the downstream. The reason for $Nu - Ra$ correlation closer to laminar scaling factor is that most heat transfer happens in the upstream of the vertical boundary layer where it is almost a laminar flow.

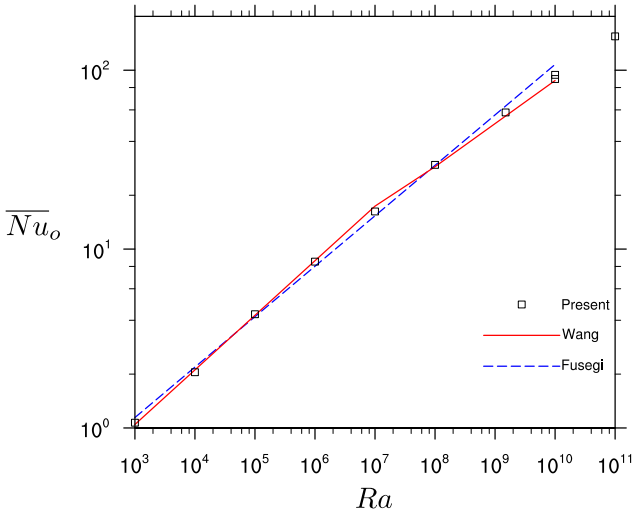

Fig. 14. Time averaged overall Nusselt number for the Rayleigh number range: $10^3 \le Ra \le 10^{11}$. The two data points at $Ra = 1.0 \times 10^{10}$ case represent results from two resolutions, as shown in Table 2, with the higher resolution giving a higher Nu value.

As pointed out in the previous sections, the flow insides the vertical boundary layer transitions from steady to time-dependent flows at the height $x = 0.7h$ for $Ra = 1.5 \times 10^9$ and $Ra = 1.0 \times 10^{10}$. For $Ra = 1.0 \times 10^{11}$ the transition point is moved to $x = 0.65h$. To distinguish the heat transfer behavior of upstream and downstream, we compute the mean Nusselt number for upstream and downstream respectively. Table 4 shows Nusselt number for upstream $\overline{Nu}_{up}$ which is integrate from $x = 0$ to $x = 0.7h$ for two lower Rayleigh numbers, and integrate from $x = 0$ to $x = 0.65h$ for $Ra = 1.0 \times 10^{11}$. Even with this domain separation, both $\overline{Nu}_{up}$ and $\overline{Nu}_{down}$ are close to classical laminar scaling of $Ra^{1/4}$. This implies that the local transition to turbulent flow here has a negligible effect on the heat transfer rate, due to a very limited domain and the constraint of the top and bottom walls.

4. Conclusion

A set of direct numerical simulations for natural convection flow in a differentially heated cubical cavity are performed, with the goal to improve our understanding of flow transition insides the vertical boundary layer adjacent to isothermal walls and its influence on heat transfer rate. The Rayleigh number range considered ($Ra = 1.5 \times 10^9$ to $Ra = 1.0 \times 10^{11}$) extends these studied in the literature. A three dimensional DUGKS code using domain decomposition and MPI is created and verified by comparing results with reference works at $Ra = 10^7$. Specifically, an improved treatment of temperature and velocity boundary conditions is proposed, based on a consistency consideration with the Chapman-Enskog approximation.

To specify the transition location, several statistics are measured. Discernible different behaviors of the upstream flow and the downstream flow are observed in the time traces of temperature and velocity. While the temperature and velocity remain essentially constant in the upstream, fluctuations are observed in the downstream region. The spectra of velocity time traces also show that the velocity fluctuations spread out to high frequencies in the downstream region. The upstream insides the boundary layer remains laminar until a transition location, and the vortices start to eject in the downstream yielding quasi-periodic or turbulent flows. With the increase of the Rayleigh number, the downstream of the thermal boundary layer becomes turbulent eventually.

Time-averaged velocity and temperature profiles are obtained. When scaled by laminar thermal boundary thickness scaling, almost identical profiles are obtained for the upstream region, and the discrepancies appear downstream of the transition location ($x = 0.65h$ to $0.7h$ depending on Ra). The turbulent fluctuation statistics in the mid-plane also confirm that the transition location for two lower Rayleigh numbers is at $x = 0.7h$, while for $Ra = 1.0 \times 10^{11}$ the transition location is approximately $x = 0.65h$. The scalings of heat transfer rate in the upstream and the downstream are also different. As the main part of the vertical boundary layer is laminar, the time-average mean Nusselt number for the hot wall is closer to laminar scaling $Ra^{1/4}$. The local transition to turbulent flow observed at high Ra numbers observed in the simulation was found to have a negligible effect on the heat transfer rate, perhaps due to a very limited domain and the constraint of the top and bottom walls.

Despite the efforts we made here for simulating natural convection flows at high Rayleigh numbers in the three-dimensional cavity, three-dimensional flow structures are far from fully explored. Especially for turbulent natural convection flow in a cavity, it requires the significant computational resources to obtain accurate statistics. Further research is thus needed in this direction.

Declaration of Competing Interest

The authors declare that they have no known competing financial interests or personal relationships that could have appeared to influence the work reported in this paper.

CRediT authorship contribution statement

Xin Wen: Conceptualization, Data curation, Formal analysis, Writing - original draft, Writing - review & editing. **Lian-Ping Wang:** Conceptualization, Methodology, Writing - review & editing, Resources, Funding acquisition. **Zhaoli Guo:** Conceptualization, Writing - review & editing. **Dauren B. Zhakebayev:** Funding acquisition.

Acknowledgments

This work has been supported by the U.S. National Science Foundation (CNS-1513031, CBET-1706130), the National Natural Science Foundation of China (91852205, 11988102, 91741101 & 11961131006), Kazakhstan Ministry of Education and Science (AP05132121), the National Numerical Wind Tunnel program, Guangdong Provincial Key Laboratory of Turbulence Research and Applications (2019B21203001), Guangdong-Hong Kong-Macao Joint Laboratory for Data-Driven Fluid Mechanics and Engineering Applications(2020B1212030001), Shenzhen Science & Technology Program (Grant No. KQTD20180411143441009), and Guangdong Science & Technology Program (2020B1212030001). Computing resources are provided by the Center for Computational Science and Engineering of Southern University of Science and Technology and by National Center for Atmospheric Research (CISL-UDEL0001).

Appendix A. Chapman-Enskog analysis of boundary condition

For the mesoscopic method used here, it is crucial to apply appropriate boundary condition to the unknown distribution functions near a wall. For the current double distribution function model, velocity and temperature boundary condition should be applied to $f(\boldsymbol{x}_w, \boldsymbol{\xi}_\alpha, t)$ and $g(\boldsymbol{x}_w, \boldsymbol{\xi}_\alpha, t)$, respectively. It is important to point out that the boundary condition should be fully consistent with the Chapman-Enskog approximation. Based on the Chapman-Enskog expansion, the distribution functions can be written approximately as:

$$f = f^{eq} - \tau_\nu \left[\frac{\partial f^{eq}}{\partial t} + \frac{\partial}{\partial x_j}(\xi_j f^{eq}) \right] + \tau_\nu \frac{a_j(\xi_j - u_j)}{RT_1} f^{eq} + \mathcal{O}(\tau_\nu^2), \tag{A.1a}$$

$$g = g^{eq} - \tau_c \left[\frac{\partial g^{eq}}{\partial t} + \frac{\partial}{\partial x_j}(\xi_j g^{eq}) \right] + \mathcal{O}(\tau_c^2). \tag{A.1b}$$

Based on the Chapman-Enskog analysis we realize that the third-order moments of equilibrium $\int \xi_i \xi_j \xi_k f^{eq} d\boldsymbol{\xi}$ is needed for momentum flux evaluation, which requires third-order Hermite expansion of $f^{eq,N=3}$ and Gauss-Hermite quadrature with sixth-degree of precision. For energy equation, the second-order moments of equilibrium $\int \xi_i \xi_j g^{eq} d\boldsymbol{\xi}$ is needed for the evaluation of energy flux. As the Mach number is very small in the current work, the third-order terms can be neglected. The equilibrium distribution is expanded to the second-order as:

$$f_\alpha^{eq,N=2} = W_\alpha \rho \left[1 + \frac{\boldsymbol{\xi}_\alpha \cdot \boldsymbol{u}}{RT_1} + \frac{(\boldsymbol{\xi}_\alpha \cdot \boldsymbol{u})^2}{2(RT_1)^2} - \frac{u^2}{2RT_1} \right] + \mathcal{O}(Ma^3), \tag{A.2a}$$

$$g_\alpha^{eq,N=2} = W_\alpha T \left[1 + \frac{\boldsymbol{\xi}_\alpha \cdot \boldsymbol{u}}{RT_2} + \frac{(\boldsymbol{\xi}_\alpha \cdot \boldsymbol{u})^2}{2(RT_2)^2} - \frac{u^2}{2RT_2} \right] + \mathcal{O}(Ma^3). \tag{A.2b}$$

For temperature and velocity boundary conditions, we can derive the following equations:

$$f(\boldsymbol{\xi}_\alpha) - f(\boldsymbol{\xi}_{\tilde{\alpha}}) = (1 - \tau_\nu \frac{a_j u_j}{RT_1})(f^{eq+} - f^{eq-}) - \tau_\nu \frac{\partial}{\partial t}(f^{eq+} - f^{eq-}) - \tau_\nu \xi_{a,j} \frac{\partial}{\partial x_j}(f^{eq+} + f^{eq-}) + \tau_\nu \frac{a_j \xi_{a,j}}{RT_1}(f^{eq+} + f^{eq-}), \tag{A.3a}$$

$$g(\boldsymbol{\xi}_\alpha) - g(\boldsymbol{\xi}_{\tilde{\alpha}}) = (g^{eq+} - g^{eq-}) - \tau_c \frac{\partial}{\partial t}(g^{eq+} - g^{eq-}) - \tau_c \xi_{a,j} \frac{\partial}{\partial x_j}(g^{eq+} + g^{eq-}), \tag{A.3b}$$

$$g(\boldsymbol{\xi}_\alpha) + g(\boldsymbol{\xi}_{\tilde{\alpha}}) = (g^{eq+} + g^{eq-}) - \tau_c \frac{\partial}{\partial t}(g^{eq+} + g^{eq-}) - \tau_c \xi_{a,j} \frac{\partial}{\partial x_j}(g^{eq+} - g^{eq-}). \tag{A.3c}$$

For simplicity, we use superscript + to represent the particles ξ_α bouncing back from the wall, while the superscript - represents the particles moving in the opposite direction to ξ_α. $g^{eq+} + g^{eq-}$, $g^{eq+} - g^{eq-}$, $h^{eq+} + h^{eq-}$ and $h^{eq+} - h^{eq-}$ can be derived from the equilibrium distributions:

$$f^{eq+} + f^{eq-} = 2W_\alpha \rho \left[1 + \frac{(\boldsymbol{\xi}_\alpha \cdot \boldsymbol{u})^2}{2(RT_1)^2} - \frac{u^2}{2RT_1} \right], \tag{A.4a}$$

$$f^{eq+} - f^{eq-} = 2W_\alpha \rho \left[\frac{\boldsymbol{\xi}_\alpha \cdot \boldsymbol{u}}{RT_1}\right], \tag{A.4b}$$

$$g^{eq+} + g^{eq-} = 2W_\alpha T\left[1 + \frac{(\boldsymbol{\xi}_\alpha \cdot \boldsymbol{u})^2}{2(RT_2)^2} - \frac{u^2}{2RT_2}\right], \tag{A.4c}$$

$$g^{eq+} - g^{eq-} = 2W_\alpha T\left[\frac{\boldsymbol{\xi}_\alpha \cdot \boldsymbol{u}}{RT_2}\right]. \tag{A.4d}$$

It is important to point out that the $\frac{\partial u}{\partial t}$ and $\frac{\partial u_i}{\partial x_j}$ operation will reduce the Mach order by one order. To keep the error term to $\mathcal{O}(\tau_\nu^2, Ma^3)$, the equilibriums need to be expanded to one-order higher, namely, to the fourth-order for f^{eq} and the third-order for g^{eq}. However, all the high order terms contain u^3 and u^4, which can be canceled under the no-slip boundary condition due to derivative by parts. Thus, we did not explicitly write out the high order terms.

Substituting these expressions into Eq. (A.3a), as all walls are assumed to be no-slip in velocity, we can set $\boldsymbol{u} = \boldsymbol{0}$ to terms not related to time- or spatial- derivatives. The u^2 and u^3 terms are also eliminated due to derivative by parts, then the following results can be obtained:

$$f(\boldsymbol{\xi}_\alpha) - f(\boldsymbol{\xi}_{\bar{\alpha}}) = -2\tau_\nu W_\alpha \frac{\xi_{a,i}}{RT_1}\frac{\partial \rho u_i}{\partial t} - 2\tau_\nu W_\alpha \xi_{a,j}\frac{\partial \rho}{\partial x_j} + 2\tau_\nu W_\alpha \rho \frac{a_j \xi_{a,j}}{RT_1}. \tag{A.5}$$

The Euler equations can be used to replace the time derivative $\rho\frac{\partial u_i}{\partial t} = -\rho u_j \frac{\partial u_i}{\partial x_j} - \frac{\partial p}{\partial x_i} + a_i\rho + \mathcal{O}(\tau)$, therefore

$$f(\boldsymbol{\xi}_\alpha) - f(\boldsymbol{\xi}_{\bar{\alpha}}) = -2\tau_\nu W_\alpha \frac{\xi_{a,i}}{RT_1}\left(-RT_1\frac{\partial \rho}{\partial x_i} + \rho a_i\right) - 2\tau_\nu W_\alpha \xi_{a,j}\frac{\partial \rho}{\partial x_j} + 2\tau_\nu W_\alpha \rho \frac{a_j\xi_{a,j}}{RT_1} + \mathcal{O}(\tau_\nu^2, Ma^3). \tag{A.6}$$

Finally, we have the mesoscopic representation of the no-slip boundary condition as

$$f(\boldsymbol{\xi}_\alpha) - f(\boldsymbol{\xi}_{\bar{\alpha}}) = 0 + \mathcal{O}(\tau_\nu^2, Ma^3). \tag{A.7}$$

Substituting the g^{eq} equilibrium into Eq. (A.3b) with $\boldsymbol{u}_w = 0$, the adiabatic boundary condition can be written as:

$$g(\boldsymbol{\xi}_\alpha) - g(\boldsymbol{\xi}_{\bar{\alpha}}) = -\tau_c \frac{\partial}{\partial t}\left(2W_\alpha T\frac{\boldsymbol{\xi}_\alpha \cdot \boldsymbol{u}}{RT_2}\right) - \tau_c \xi_{a,j}\frac{\partial}{\partial x_j}(2W_\alpha T) + \mathcal{O}(\tau_c^2, Ma^3). \tag{A.8}$$

Again the Euler equations are used to replace the time derivative $\rho\frac{\partial u_i}{\partial t} = -\rho u_j \frac{\partial u_i}{\partial x_j} - \frac{\partial p}{\partial x_i} + a_i\rho + \mathcal{O}(\tau)$, to obtain

$$g(\boldsymbol{\xi}_\alpha) - g(\boldsymbol{\xi}_{\bar{\alpha}}) = -2\tau_c W_\alpha \frac{\xi_{a,i}T}{RT_2}\left(-\frac{1}{\rho}\frac{\partial \rho RT_1}{\partial x_i} + a_i\right) - 2\tau_c W_\alpha \xi_{a,j}\frac{\partial T}{\partial x_j} + \mathcal{O}(\tau_c^2, Ma^3). \tag{A.9}$$

The final result of mesoscopic representation of the adiabatic boundary condition becomes

$$g(\boldsymbol{\xi}_\alpha) - g(\boldsymbol{\xi}_{\bar{\alpha}}) = 2\tau_c W_\alpha \xi_{a,i}\left(\frac{T_1}{T_2}\frac{T}{\rho}\frac{\partial \rho}{\partial x_i} - \frac{a_i T}{RT_2} - \frac{\partial T}{\partial x_i}\right) + \mathcal{O}(\tau_c^2, Ma^3). \tag{A.10}$$

For isothermal boundary condition, we can derive the following expression from Eq. (A.3c):

$$g(\boldsymbol{\xi}_\alpha) + g(\boldsymbol{\xi}_{\bar{\alpha}}) = 2W_\alpha T - 2W_\alpha \tau_c \frac{\partial T}{\partial t} - 2W_\alpha \tau_c T \frac{\xi_{a,i}\xi_{a,j}}{RT_2}\frac{\partial u_i}{\partial x_j}. \tag{A.11}$$

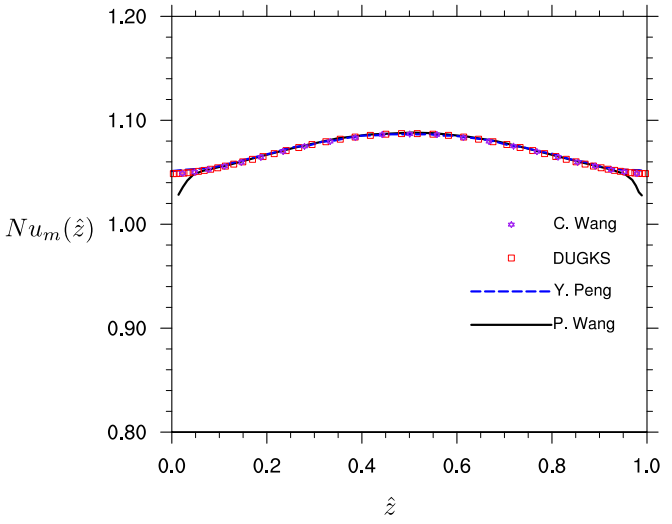

Fig. A.15. The comparison of mean Nusselt number $Nu_m(\hat{z})$ distribution among present DUGKS results and reference results Peng et al. [27]; Wang et al. [39]; Wang [21]).

Leading order energy equation is used to replace the time derivatives $\frac{\partial T}{\partial t} = -\frac{\partial T u_j}{\partial x_j} + \mathcal{O}(\tau)$. Then, the final result for isothermal wall is

$$g(\boldsymbol{\xi}_\alpha) + g(\boldsymbol{\xi}_{\bar{\alpha}}) = 2W_\alpha T\left(1 + \tau_c\frac{\partial u_j}{\partial x_j} - \frac{\tau_c \xi_{a,i}\xi_{a,j}}{RT_2}\frac{\partial u_i}{\partial x_j}\right) + \mathcal{O}(\tau_c^2, Ma^3). \tag{A.12}$$

In summary, for no-slip boundary condition, the standard "bounce-back" is consistent with the Chapman-Enskog analysis. However, for temperature boundary conditions, most literature works only keep the $\mathcal{O}(1)$ term. In fact, the $\mathcal{O}(\tau_c)$ terms have influence on the heat flux at the boundary. In actual implementation, the derivatives of hydrodynamic variables can be evaluated approximately using the values from last time step. To show that the temperature boundary condition can be accurately implemented by the current kinetic boundary condition, we performed a simulation of natural convection in an air-filled cubical cavity with $Ra = 1.0 \times 10^3$. Fig. A.15 shows the mean Nusselt number distribution along the z-direction, where $Nu_m(\hat{z})$ is defined as:

$$Nu_m(\hat{z}) = \int_0^1 \frac{\partial \theta(\hat{x}, \hat{z})}{\partial \hat{y}}\bigg|_{\hat{y}=0} d\hat{x}. \tag{A.13}$$

We compared the mean Nusselt distribution of the current DUGKS results and those from the literature [21,27,39]. Our results agree well with the conventional CFD results of Wang et al. [39] and LBM results of Peng et al. [27]. The results provided by Wang [21] is obtained using the DUGKS scheme with only $\mathcal{O}(1)$ boundary condition implementation. It is obvious that the boundary condition is improved using our current kinetic boundary condition including the $\mathcal{O}(\tau_c)$ terms.

To further confirm the convergence order of the DUGKS, we performed a series of two-dimensional simulations of natural convection in a square cavity at $Ra = 1.0 \times 10^3$ with different meshes. Simulations are conducted with meshes $20 \times 20, 40 \times 40, 80 \times 80, 160 \times 160, 320 \times 320$ and the CFL numbers are adjusted to keep the time step constant accordingly. The L_2 erros in temperature and velocity field are measured in Table A.5, where the L_2 error is defined as:

$$E(\phi) = \frac{\sqrt{\sum_{x,y}|\phi(x,y,t) - \phi_e(x,y,t)|^2}}{\sqrt{\sum_{x,y}|\phi_e(x,y,t)|^2}} \tag{A.14}$$

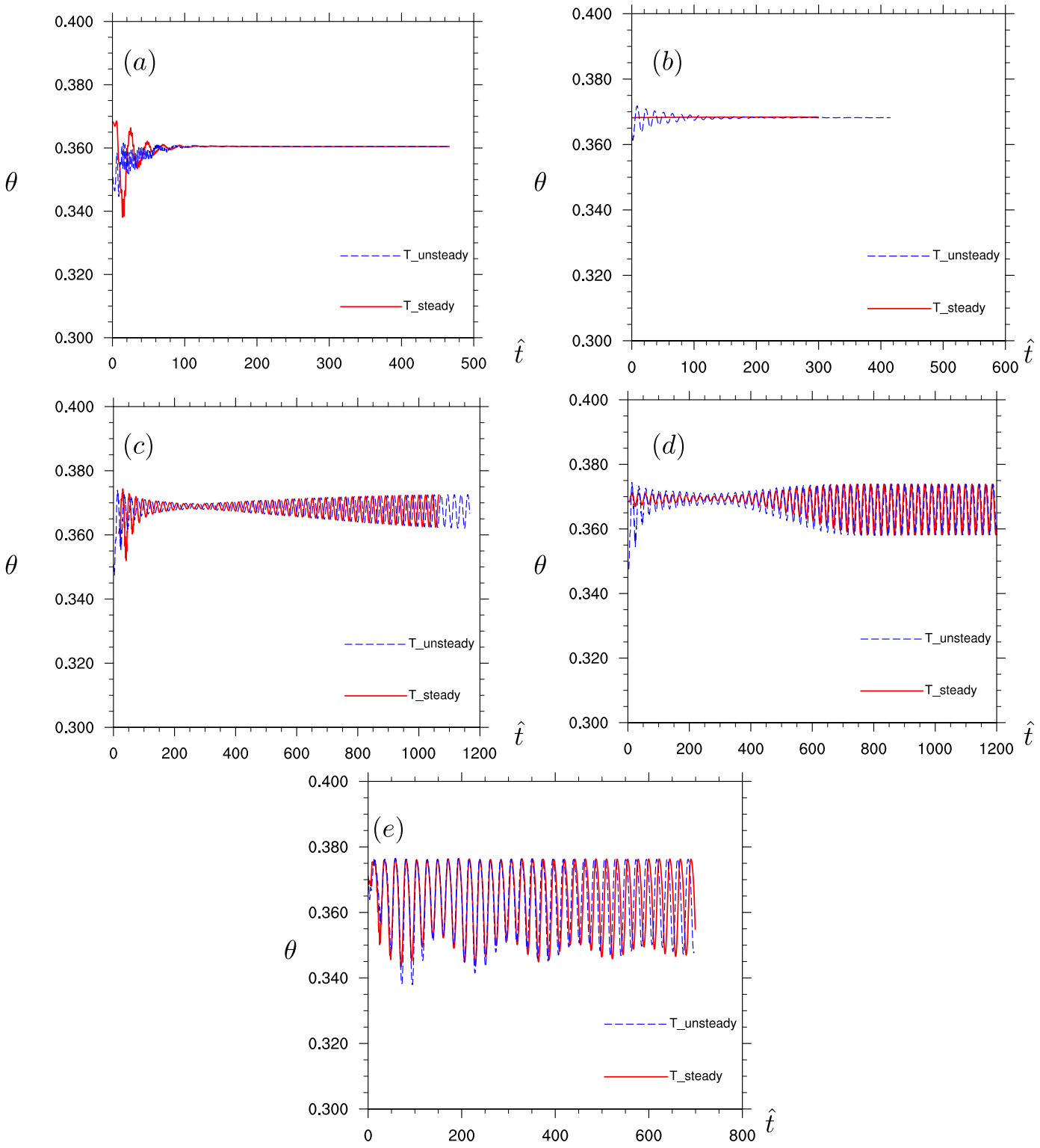

Fig. A.16. Time trace of temperature θ at location $(\hat{x}, \hat{y}) = (0.88, 0.15)$ for: (a) $Ra = 1.6 \times 10^8$;(b) $Ra = 1.8 \times 10^8$; (c) $Ra = 1.82 \times 10^8$; (d) $Ra = 1.84 \times 10^8$; (e) $Ra = 2.0 \times 10^8$.

where $\phi = \theta$ or $\hat{\boldsymbol{u}}$, and ϕ_e is the benchmark value with the mesh 320×320. At least second-order convergence of the DUGKS is confirmed.

Besides the steady natural convection simulation, we also validate our code by calculating the critical Rayleigh number of transition to unsteady flow regime for two-dimensional natural convection in a square cavity. A set of simulations of two-dimensional natural convection with non-uniform 500×500 meshes are performed. The non-uniformity parameter is set to be $S = 3$, and the minimum grid spacing is $\Delta x_{\min} = 6.0219 \times 10^{-4} L$. Fig. A.16 shows time trace of temperature at monitoring point for the simulation with five different Rayleigh numbers. The red line represents the time integration was started from the steady flow of the case $Ra = 1.8 \times 10^8$ and the blue dash line represents the simulation was started from the unsteady solution of the case $Ra = 2.0 \times 10^8$. Steady results are obtained for the cases $Ra = 1.6 \times 10^8$ and $Ra =$

Table A.5
Error and convergence order in velocity and temperature.

N	20	40	80	160
$E(\theta)$	5.3583×10^{-3}	9.2810×10^{-4}	1.5528×10^{-4}	2.3295×10^{-5}
order	-	2.5294	2.5794	2.7368
$E(\tilde{\boldsymbol{u}})$	4.3024×10^{-2}	7.2083×10^{-3}	1.2445×10^{-3}	2.1210×10^{-4}
order	-	2.5774	2.5341	2.5527

1.8×10^8, for both initial conditions. For the cases $Ra = 1.82 \times 10^8$ and $Ra = 1.84 \times 10^8$, it shows that the solution first experiences damped oscillations and then reaches periodic oscillations. With these high resolution results, the critical Rayleigh number would be between 1.80×10^8 and 1.82×10^8, which is consistent with the the Le Quéré and Behnia result for Ra_c, $Ra_c = (1.82 \pm 0.01) \times 10^8$. We also note that the amplitude of oscillations increases with Ra for $Ra \geq 1.82 \times 10^8$.

Appendix B. Order of accuracy test

To validate the second-order accuracy of our scheme in both space and time, we simulated the unsteady 2D Taylor-Green vortex flow in a square domain. The Taylor-Green vortex flow is an exact solution of the Navier-Stokes equation in a two-dimensional periodic domain, representing the viscous decay process of a vortical flow. The velocity and pressure fields of this unsteady flow are given as:

$$u(x, y, t) = -U_0 \cos\left(\frac{2\pi x}{L}\right) \sin\left(\frac{2\pi y}{L}\right) e^{-\frac{8\pi^2 \nu t}{L^2}}, \tag{B.1a}$$

$$v(x, y, t) = U_0 \cos\left(\frac{2\pi y}{L}\right) \sin\left(\frac{2\pi x}{L}\right) e^{-\frac{8\pi^2 \nu t}{L^2}}, \tag{B.1b}$$

$$p(x, y, t) = -\frac{1}{2} U_0^2 \cos\left[\frac{2\pi}{L}(x - y)\right] \cos\left[\frac{2\pi}{L}(x + y)\right] e^{-\frac{16\pi^2 \nu t}{L^2}}, \tag{B.1c}$$

where ν is the shear viscosity. In order to use the analytical solution as the rigorous benchmark, we must initialize the distribution functions carefully to be fully consistent with the hydrodynamic velocity and pressure fields. In the DUGKS simulation, the initial distributions are generated by iteration as follows:

1. Begin with the initial distribution function defined as $f(\boldsymbol{x}, \boldsymbol{\xi}_\alpha, 0) = f_\alpha^{eq}[\rho(\boldsymbol{x}, 0), \boldsymbol{u}(\boldsymbol{x}, 0)]$, where $\rho(\boldsymbol{x}, 0) = p(\boldsymbol{x}, 0)/c_s^2$.

$$f_\alpha^{eq,N=2} = W_\alpha \rho \left\{1 + \frac{\boldsymbol{\xi}_\alpha \cdot \boldsymbol{u}}{RT_1} + \frac{(\boldsymbol{\xi}_\alpha \cdot \boldsymbol{u})^2}{2(RT_1)^2} - \frac{u^2}{2RT_1}\right\} + O(Ma^3) \tag{B.2}$$

2. Evolve the distribution function for one time step with DUGKS. Update the hydrodynamic variable and denote them as $\rho(\boldsymbol{x}, \Delta t)$ and $\boldsymbol{u}(\boldsymbol{x}, \Delta t)$.
3. Based on the Chapman-Enskog expansion, the distribution function can be written as follows:

$$f_\alpha = f_\alpha^{eq} - \tau_\nu \left[\frac{\partial f_\alpha^{eq}}{\partial t} + \frac{\partial}{\partial x_j}(\xi_j f_\alpha^{eq})\right] + \tau_\nu \frac{a_j(\xi_j - u_j)}{RT_1} f_\alpha^{eq} + \mathcal{O}(\tau_\nu^2) \tag{B.3}$$

With the unexpanded form of the equilibrium distribution and the Euler equation, the distribution function can be written as:

$$\begin{aligned} f_\alpha &= f_\alpha^{eq}\left[1 + \tau_\nu\left(\frac{\partial u_i}{\partial x_i} - \frac{c_i c_j}{RT_1}\frac{\partial u_i}{\partial x_j}\right)\right] + O(\tau_\nu^2) \\ &= f_\alpha^{eq} + \tau_\nu f_\alpha^{(1)} + \mathcal{O}(\tau_\nu^2). \end{aligned} \tag{B.4}$$

Table B.6
L_2 Errors and convergence order in velocity and pressure with different mesh sizes ($dt = 1.0 \times 10^{-5}$).

N	20	40	80	160
$\frac{U_0 dt}{dx}$	2×10^{-4}	4×10^{-4}	8×10^{-4}	1.6×10^{-3}
$\frac{c_s dt}{dx}$	2×10^{-3}	4×10^{-3}	8×10^{-3}	1.6×10^{-2}
$E(\boldsymbol{u})$	9.343971E-3	2.187037E-3	5.718380E-4	1.371459E-4
order	-	2.0951	1.9353	2.0599
$E(p)$	2.562765E-2	7.614341E-3	1.927406E-3	4.033651E-4
order	-	1.7509	1.9821	2.2565

Table B.7
L_2 Errors and convergence order in velocity and pressure with different time step sizes (fixed CFL number).

dt	2.0×10^{-3}	1.0×10^{-3}	5.0×10^{-4}	2.5×10^{-4}
N	20	40	80	160
$\frac{U_0 dt}{dx}$	0.04	0.04	0.04	0.04
$\frac{c_s dt}{dx}$	0.4	0.4	0.4	0.4
$E(\boldsymbol{u})$	5.798385E-1	1.059667E-1	1.384611E-2	1.317480E-3
order	-	2.4520	2.9361	3.3936
$E(p)$	8.176620E-1	1.914017E-1	2.716178E-2	2.573582E-3
order	-	2.0949	2.8170	3.3997

where $f_\alpha^{(1)} = f_\alpha^{eq}\left(\frac{\partial u_i}{\partial x_i} - \frac{c_i c_j}{RT_1}\frac{\partial u_i}{\partial x_j}\right)$. Then we can construct a new set of the initial distribution as:

$$\tau_\nu f_\alpha^{(1)}(\boldsymbol{x}, 0) \approx f_\alpha(\boldsymbol{x}, \Delta t) - f_\alpha^{eq}[\rho(\boldsymbol{x}, \Delta t), \boldsymbol{u}(\boldsymbol{x}, \Delta t)] + \mathcal{O}(\tau_\nu^2), \tag{B.5a}$$

$$f_\alpha(\boldsymbol{x}, 0) = \tau_\nu f_\alpha^{(1)}(\boldsymbol{x}, 0) + f_\alpha^{eq}[\rho(\boldsymbol{x}, \Delta t), \boldsymbol{u}(\boldsymbol{x}, 0)]. \tag{B.5b}$$

4. Repeat step 2 and 3 until the pressure and stress fields at the initial time converge.

The parameters used in the simulations are: $Re = 1000$, $\nu = 0.001$, $L = 1.0$, $U_0 = 1.0$, $RT = 100$. We compare the velocity profiles and pressure profiles at two dimensionless times (not shown) with the analytical solution, and find that the numerical solution agrees well with the theoretical solution. To confirm the convergence order of DUGKS, a set of simulations with different resolutions and time steps are performed. The L_2 errors

$$L_2 = \frac{\sqrt{\sum_{i,j} |V_N(i, j) - V_T(i, j)|^2}}{N^2} \tag{B.6}$$

where V represents velocity or pressure. The L_2 errors are shown in Tables B.6 and B.7, along with the resulting order of accuracy. In Table B.6, time step size (as viewed by the conventional CFL number and the kinetic CFL number $c_s dt/dx$) is kept very small so the L_2 errors represent mainly the space discretization errors, the order of accuracy is around 2. In Table B.7, we fixed the kinetic CFL number to 0.4 so both the time discretization error and space discretization error are present, the realized order of accuracy is between 2 to 3. Since the requirement that $c_s dt/dx < 1$ implies that we cannot isolate space discretization error from the time discretization error in DUGKS. Overall, Tables B.6 and B.7 together demonstrate the second-order accuracy in both space and time.

References

[1] J.H. Lienhard, A Heat Transfer Textbook, fourth edition, Phlogiston Press, 2015.
[2] E. Bodenschatz, W. Pesch, G. Ahlers, Recent developments in Rayleigh-Bénard convection, Annu. Rev. Fluid Mech. 32 (1) (2000) 709–778.
[3] D. Lohse, K.Q. Xia, Small-scale properties of turbulent Rayleigh-Bénard convection, Annu. Rev. Fluid Mech. 42 (1) (2010) 335–364.
[4] G.D. Mallinson, G. de Vahl Davis, Three-dimensional natural convection in a box: a numerical study, J. Fluid Mech. 83 (1977) 1–31.

[5] G. de Vahl Davis, I.P. Jones, Natural convection in a square cavity: a comparison exercise, Int. J. Numer. Methods Fluids 3 (1983) 227–248.
[6] J. Salat, S. Xin, P. Joubert, A. Sergent, F. Penot, P.L. Quéré, Experimental and numerical investigation of turbulent natural convection in a large air-filled cavity, Int. J. Heat Fluid Flow 25 (2004) 824–832.
[7] Y.S. Tian, T.G. Karayiannis, Low turbulence natural convection in an air filled square cavity part 1: the thermal and fluid flow fields, Int. J Heat Mass Transf. 43 (2000) 849–866.
[8] Y.S. Tian, T.G. Karayiannis, Low turbulence natural convection in an air filled square cavity Part 2: the turbulence quantities, Int. J. Heat Mass Transf. 43 (2000) 867–884.
[9] P.L. Quéré, Accurate solutions to the square thermally driven cavity at high Rayleigh number, Comput. Fluids 20 (1991) 29–41.
[10] S. Paolucci, D.R. Chenoweth, Transition to chaos in a differentially heated vertical cavity, J. Fluid Mech. 201 (1989) 379–410.
[11] R.J.A. Janssen, R.A.W.M. Henkes, Influence of Prandtl number on instability mechanism and transition in a differentially heated square cavity, J. Fluid Mech. 290 (1995) 319–344.
[12] P.L. Quéré, M. Behnia, From onset of unsteadiness to chaos in a differentially heated square cavity, J. Fluid Mech. 359 (1998) 81–107.
[13] Y.L. Zhao, C.W. Lei, J.C. Patterson, Transition of natural convection boundary layer-a revisit by Bicoherence analysis, Int. Commun. Heat Mass Transf. 58 (2014) 147–155.
[14] Y.L. Zhao, C.W. Lei, J.C. Patterson, Natural transition in natural convection boundary layers, Int. Commun. Heat Mass Transf. 76 (2016) 366–375.
[15] R. Janssen, S. Armfield, Stability properties of the vertical boundary layers in differentially heated cavities, Int. J. Heat Fluid Flow 17 (1996) 547–556.
[16] T. Fusegi, J.M. Hyun, K. Kuwahara, B. FAROUK, A numerical study of three-dimensional natural convection in a differentially heated cubical enclosure, Int. J. Heat Mass Transf. 34 (1991) 1543–1557.
[17] E. Tric, G. Labrosse, M. Betrouni, A first incursion into the three-dimensional structure of natural convection of air in a differentially heated cubic cavity, from accurate numerical solutions, Int. J. Heat Mass Transf. 43 (2000) 4043–4056.
[18] T. Fusegi, J.M. Hyun, K. Kuwahara, Three-dimensional simulations of natural convection in a sidewall-heated cube, Int. J. Numer. Meth. Fluids 13 (1991) 857–867.
[19] R.J.A. Janssen, R.A.W.M. Henkes, Instabilities in three-dimensional differentially-heated cavities with adiabatic horizontal walls, Phys. Fluids 8 (1996) 62–74.
[20] G. Labrosse, E. Tric, H. Khallouf, M. Betrouni, A direct(pseudo-spectral) solver of the two-/three-dimensional stokes problem: transition to unsteadiness of natural-convection flow in a differentially heated cubical cavity, Numer. Heat Transf. 31 (1997) 261–276.
[21] P. Wang, Discrete unified gas-kinetic scheme for incompressible flows and its applications, Huazhong University of Science and Technology, 2016 phd thesis.
[22] P. Wang, Y. Zhang, Z. Guo, Numerical study of three-dimensional natural convection in a cubical cavity at high Rayleigh numbers, Int. J. Heat Mass Transf. 113 (2017) 217–228.
[23] F.X. Trias, M. Soria, A. Oliva, C.D. Pérez-segarra, Direct numerical simulations of two- and three-dimensional turbulent natural convection flows turbulent natural flows in a differentially heated cavity of aspect ratio 4, J. Fluid Mech. 586 (1) (2007) 259–293.
[24] F.X. Trias, A. Gorobets, M. Soria, A. Oliva, Direct numerical simulation of a differentially heated cavity of aspect ratio 4 with Rayleigh numbers up to 10^{11} - Part 1: numerical methods, Int. J. Heat Mass Transf. 53 (2010) 665–673.
[25] F.X. Trias, A. Gorobets, M. Soria, A. Oliva, Direct numerical simulation of a differentially heated cavity of aspect ratio 4 with Rayleigh numbers up to 10^{11} - Part 2: Heat transfer and flow dynamics, Int. J. Heat Mass Transf. 53 (2010) 674–683.
[26] X. Shan, Simulation of Rayleigh-Bénard convection using a lattice Boltzmann method, Phys. Rev. E 55(3) (1997) 2780–2788.
[27] Y. Peng, C. Shu, Y.T. Chew, A 3D incompressible thermal lattice Boltzmann model and its application to simulate natural convection in a cubic cavity, J. Comput. Phys. 193 (2003) 260–274.
[28] A. Xu, L. Shi, H.D. Xi, Lattice Boltzmann simulations of three-dimensional thermal convective flows at high Rayleigh number, Int. J. Heat Mass Transf. 140 (2019) 359–370.
[29] Z. Guo, K. Xu, R. Wang, Discrete unified gas kinetic scheme for all Knudsen number flows: low-speed isothermal case, Phys. Rev. E 88 (2013) 033305.
[30] P. Wang, L.H. Zhu, Z.L. Guo, K. Xu, A comparative study of LBE and DUGKS methods for nearly incompressible flows, Commun. Comput. Phys. 17 (2015) 657–681.
[31] P. Wang, L.P. Wang, Z.L. Guo, Comparison of the LBE and DUGKS methods for DNS of decaying homogeneous isotropic turbulence, Phys. Rev. E 94 (2016) 043304.
[32] Y.T. Bo, P. Wang, Z.L. Guo, L.P. Wang, DUGKS simulations of three-dimensional Taylor-Green vortex flow and turbulent channel flow, Comput. Fluids 155 (1) (2017) 9–21.
[33] P.K. Kundu, I.M. Cohen, D.R. Dowling, Fluid Mechanics, fourth edition, Academic Press, 2008, pp. 124–128.
[34] P. Wang, S. Tao, Z. Guo, A coupled discrete unified gas-kinetic scheme for Boussinesq flows, Comput. Fluids 120 (2015) 70–81.
[35] K. Xu, S. Liu, Rayleigh-Bénard simulation using the gas-kinetic Bhatnagar–Gross-Krook scheme in the incompressible limit, Phys. Rev. E 60(1) (1999) 464–470.
[36] G. Grötzbach, Spatial resolution requirement for direct numerical simulation of the Rayleigh-Bénard convection, Int. J. Numer. Meth. Fluids 49 (1983) 241–264.
[37] O. Shishkina, R.J. Stevens, S. Grossmann, D. Lohse, Boundary layer structure in turbulent thermal convection and its consequences for the required numerical resolution, N. J. Phys. 12 (2010) 075022.
[38] S. Xin, P.L. Quéré, Direct numerical simulations of two-dimensional chaotic natural convection in a differentially heated cavity of aspect ratio 4, J. Fluid Mech. 304 (1995) 87–118.
[39] C.A. Wang, H. Sadat, C. Prax, A new meshless approach for three dimensional fluid flow and related heat transfer problems, Comput. Fluids 69 (2012) 136–146.